EUROPEAN LABORATORY FOR PARTICLE PHYSICS

CERN-SPSC/99-26
SPSC/P311
August 30, 1999

# PROPOSAL

# SEARCH FOR $\nu_\mu \rightarrow \nu_e$ OSCILLATION AT THE CERN PS

M.Guler, M.Serin-Zeyrek, R.Sever, P.Tolun, M.T.Zeyrek
METU - Ankara - Turkey

N.Armenise, M.G.Catanesi, M.T.Muciaccia, E.Radicioni, P.Righini, S.Simone
Università degli Studi e Sezione INFN, Bari - Italy

K.Winter
Humboldt-Universitaet - Berlin - Germany

R.Maschuw
University of Bonn - Germany

B.Van de Vyver, P.Vilain, G.Wilquet
IIHE - Brussels - Belgium

B.Saitta
Università degli Studi e Sezione INFN, Cagliari - Italy

J.R.Batley, D.J.Munday, D.R.Ward, C.P.Ward
University of Cambridge - UK

S.Bunyatov, O.Klimov, A.Krasnoperov, Yu.Nefedov, B.Popov, V.Tereshchenko
JINR - Dubna -Russia

E.Di Capua, G.Zavattini
Università degli Studi e Sezione INFN, Ferrara - Italy

D.Autiero, L.Camilleri, A.DeSanto, L.Di Lella, M.Doucet, F.Dydak,
J.P.Fabre, A.Grant, L.Linssen, J.Panman, I.M.Papadopoulos,
E.Pesen, R.Petti, S.Ricciardi, P.Zucchelli
CERN - Geneva - Switzerland

D.Favart, J.Govaerts, G.Gregoire
UCL - Louvain-la-Neuve - Belgium

D.Levin, S.McKee, G.Tarle, R.Thun
University of Michigan, Ann Arbor, MI 48109 USA

M. Bonesini, M. Calvi, P.Negri, M. Paganoni, A. Pullia, S.Ragazzi,
N.Redaelli, T.Tabarelli de Fatis, F.Terranova
Università degli Studi e Sezione INFN, Milano - Italy

S.Gninenko, N.Goloubev, M.Kirsanov, A.Kovzelev, A. Polarush, A.Toropin
INR - Moscow - Russia

V.Palladino
Università Federico II e Sezione INFN, Napoli - Italy

M.Baldo-Ceolin, D.Gibin, A.Guglielmi, M.Laveder, M.Mezzetto, A.Pepato
Università G. Galilei e Sezione INFN, Padova - Italy

J.Dumarchez, F.Vannucci
(subject to IN2P3 approval)
Universite' de Paris VI et VII - Paris - France

D.De Pedis, U.Dore, A.Frenkel, P.F.Loverre (*), L.Ludovici, A.Maslennikov,
R.Santacesaria, A.Satta, F.Spada
Università "La Sapienza" e Sezione INFN, Roma - Italy

D.Orestano, F.Pastore
Università di Roma Tre e Sezione INFN, Roma - Italy

D.O.Caldwell, S.J.Yellin
University of California - Santa Barbara -California - USA

D.Kolev, R.Tsenov
St. Kliment Ohridski University of Sofia -Sofia - Bulgaria

F.Avignone, S.Mishra, C.Rosenfeld
University of South Carolina - Columbia - USA

M.Barone, G.Conforto, C.Grimani
Università di Urbino e Sezione INFN, Urbino - Italy

J.J. Gomez-Cadenas, C.Gonzalez, J. Velasco
University of Valencia - Spain

(*) Contactperson

# Contents

**1 Introduction and motivation** **5**

**2 The Experiment** **7**
2.1 Principles and capabilities of the experiment . . . . . . . . . . . . . . . 7
2.2 Experimental layout . . . . . . . . . . . . . . . . . . . . . . . . . . . . 7
2.3 Sensitivity to oscillations . . . . . . . . . . . . . . . . . . . . . . . . . . 8

**3 The neutrino beam** **12**
3.1 Requirements on the PS neutrino beam . . . . . . . . . . . . . . . . . 12
3.2 The PS neutrino beam line . . . . . . . . . . . . . . . . . . . . . . . . 12
3.3 Requirements on proton intensity . . . . . . . . . . . . . . . . . . . . 13
3.4 Beam simulation . . . . . . . . . . . . . . . . . . . . . . . . . . . . . . 15
3.5 Costs of beam reactivation . . . . . . . . . . . . . . . . . . . . . . . . 21

**4 The experimental halls** **22**
4.1 General layout . . . . . . . . . . . . . . . . . . . . . . . . . . . . . . . 22
4.2 Hall 181 . . . . . . . . . . . . . . . . . . . . . . . . . . . . . . . . . . 22
4.3 Hall 182 . . . . . . . . . . . . . . . . . . . . . . . . . . . . . . . . . . 23
4.4 Cost estimates . . . . . . . . . . . . . . . . . . . . . . . . . . . . . . . 24

**5 The Detector** **26**
5.1 Introduction . . . . . . . . . . . . . . . . . . . . . . . . . . . . . . . . 26
5.2 The scintillator bar . . . . . . . . . . . . . . . . . . . . . . . . . . . . 26
5.3 The Basic Unit . . . . . . . . . . . . . . . . . . . . . . . . . . . . . . 27
5.4 The Detector Module . . . . . . . . . . . . . . . . . . . . . . . . . . . 28
5.5 End-system . . . . . . . . . . . . . . . . . . . . . . . . . . . . . . . . 29
5.6 Detector performance . . . . . . . . . . . . . . . . . . . . . . . . . . . 31
5.7 Calibration of the electron energy scale . . . . . . . . . . . . . . . . . 35
5.8 Construction time scale and costs . . . . . . . . . . . . . . . . . . . . 37

**6 The photodetectors** **40**
6.1 Description . . . . . . . . . . . . . . . . . . . . . . . . . . . . . . . . 40
6.2 Uniformity and crosstalk . . . . . . . . . . . . . . . . . . . . . . . . . 40
6.3 High voltage system . . . . . . . . . . . . . . . . . . . . . . . . . . . 42

**7 Readout electronics** **43**
7.1 Description . . . . . . . . . . . . . . . . . . . . . . . . . . . . . . . . 43
7.2 Choice of the front-end chip . . . . . . . . . . . . . . . . . . . . . . . 43
7.3 Electronic boards and VME modules . . . . . . . . . . . . . . . . . . 44
7.4 Cost and time estimates . . . . . . . . . . . . . . . . . . . . . . . . . 44

**8 DAQ** **47**
8.1 Introduction . . . . . . . . . . . . . . . . . . . . . . . . . . . . . . . . 47
8.2 Readout crates and Data Volumes . . . . . . . . . . . . . . . . . . . . 47
8.3 Calibration . . . . . . . . . . . . . . . . . . . . . . . . . . . . . . . . . 47
    8.3.1 Electronics calibration . . . . . . . . . . . . . . . . . . . . . . . 47
    8.3.2 Absolute calibration . . . . . . . . . . . . . . . . . . . . . . . . 49
8.4 Network Topology . . . . . . . . . . . . . . . . . . . . . . . . . . . . 49

8.5 Main DAQ process . . . . . . . . . . . . . . . . . . . . . . . . . . . 50
8.6 Database . . . . . . . . . . . . . . . . . . . . . . . . . . . . . . . . 50
8.7 Total Data Volume . . . . . . . . . . . . . . . . . . . . . . . . . . 52

**9 Signal and background** **53**
9.1 Low energy neutrino interactions . . . . . . . . . . . . . . . . . . 53

**10 Event simulation and selection** **57**
10.1 The detector simulation . . . . . . . . . . . . . . . . . . . . . . . 57
10.2 Event simulation and detector response . . . . . . . . . . . . . . . 57
10.3 Event selection . . . . . . . . . . . . . . . . . . . . . . . . . . . . 61

**11 Sensitivity to Oscillation** **65**
11.1 $\boldsymbol{\nu_\mu \rightarrow \nu_e}$ oscillations in appearance mode . . . . . . . . . . . . . . . 65
11.2 $\boldsymbol{\nu_\mu \rightarrow \nu_x}$ oscillations in disappearance mode . . . . . . . . . . . . . . 66
11.3 The measurement of $\boldsymbol{\Delta m^2}$ and $\boldsymbol{sin^2 2\theta}$ . . . . . . . . . . . . . . . . . . 70

**12 Summary of cost** **72**

**13 Construction time scale** **73**

# 1 Introduction and motivation

Strong experimental evidence has been reported for deficits of both solar $\nu_{\mathrm{e}}$ [1, 2] and atmospheric $\nu_\mu$ [2, 3]. Their interpretation in terms of neutrino oscillations is largely accepted.

Neutrino oscillations are an extremely interesting new phenomenon which implies a non-zero neutrino mass. It promises insight into the structure of physics beyond the standard model and might also shed some light on the understanding of CP violation. The neutrino mass scale is a question of fundamental interest in particle physics and may be cosmologically important as massive neutrinos could contribute to dark matter and to the large-scale structure of the universe.

In what can be presently viewed as the standard scenario, a $\Delta m^2$ around $10^{-3}$ $\mathrm{eV}^2$ governs the phenomena observed with atmospheric neutrinos, while a $\Delta m^2$ in the range $10^{-4}$ – $10^{-11}$ $\mathrm{eV}^2$ is responsible for the solar neutrino deficit.

Evidence for neutrino oscillations has also been presented by the LSND experiment but is presently unconfirmed. This experiment is the only one to claim evidence for the *appearance* of another neutrino flavour. Two experimentally distinct excesses of events have been reported:

- $\bar{\nu}_\mu \rightarrow \bar{\nu}_{\mathrm{e}}$ ($\bar{\nu}_\mu$ from $\mu^+$ decays at rest) [4];
- $\nu_\mu \rightarrow \nu_{\mathrm{e}}$ ($\nu_\mu$ from $\pi^+$ decays in flight) [5].

Interpreted as a two-flavour oscillation of $\nu_\mu \rightarrow \nu_{\mathrm{e}}$, these signals give the allowed region in $\Delta m^2$ *vs* $sin^2 2\theta$ shown in Fig. 1. After further data taking and numerous experimental cross-checks, LSND has confirmed their claim and even reported an increased statistical significance [6].

A large fraction of the region allowed by the LSND experiment is excluded by other experiments [7, 8, 9], but the possibility of a value of $\Delta m^2$ in the range 0.3 - 2.0 $\mathrm{eV}^2$ remains open. The KARMEN2 experiment will not be able to settle the LSND issue in a decisive manner [7].

Should the LSND result be confirmed, a radically different physics world would open up as a new mass scale of the order of 1 $\mathrm{eV}^2$ would imply a complete revision of the current oscillation scenario, most likely requiring a fourth neutrino which must be sterile since it is not seen in Z decay. It is imperative, therefore, that the LSND claim be confirmed or refuted.

At FNAL, the MiniBooNE experiment [10] has been approved in order to check the LSND result and plans to take data after the year 2001.

In view of the importance of confirming or disproving the LSND result, we propose to carry out a decisive experiment at CERN using a neutrino beam from the CERN PS and employing the near/far detector technique. The proposed experiment will run concurrently with MiniBooNE but will have entirely different systematics.

The near/far detector technique offers the possibility to study also the $\nu_\mu \rightarrow \nu_x$ disappearance channel. Should the $\nu_\mu \rightarrow \nu_{\mathrm{e}}$ signal be confirmed, this channel becomes very interesting because most models with three-neutrino mixing [11] also predict a relatively large $\nu_\mu \rightarrow \nu_\tau$ oscillation probability at the same $\Delta m^2$ value, well within the sensitivity of this experiment.

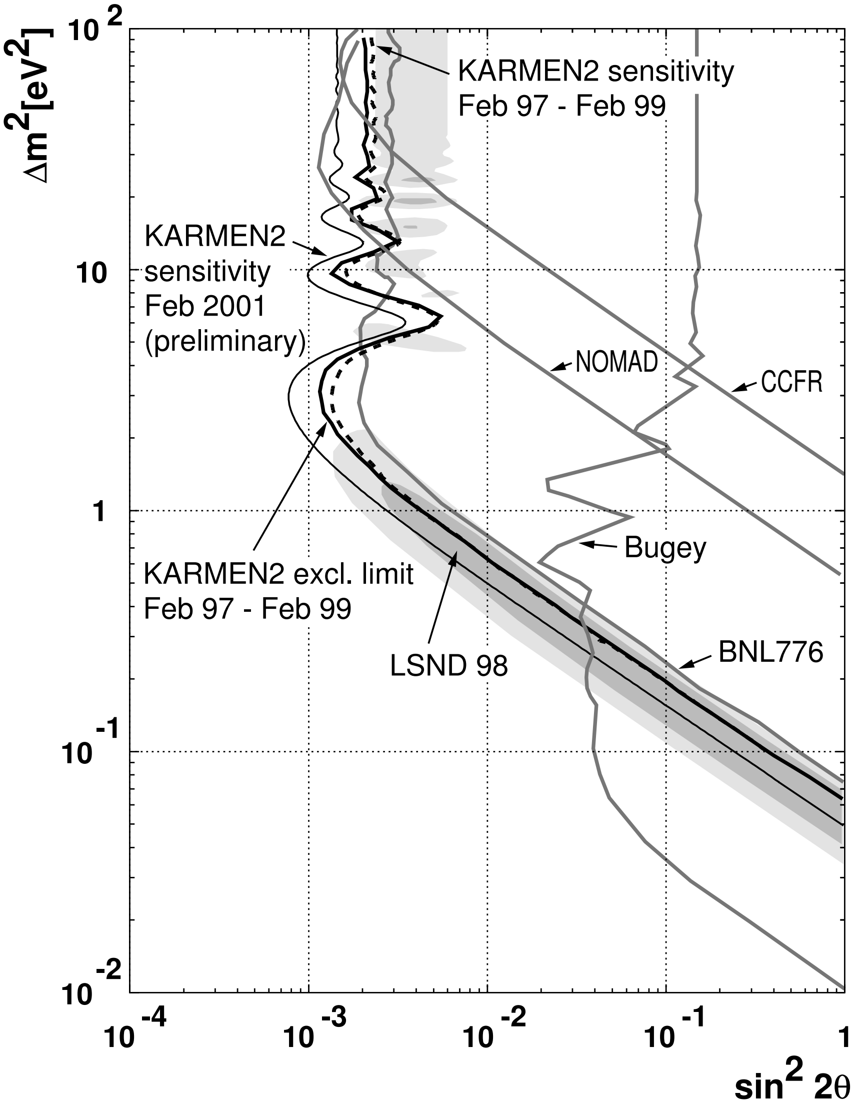

Figure 1: Regions in $\Delta m^2$ *vs* $sin^2 2\theta$ allowed by LSND and excluded by other experiments (from ref. [7]). The dark-shaded and light-shaded regions correspond to the LSND 90% and 99% likelihood regions, respectively.

# 2 The Experiment

## 2.1 Principles and capabilities of the experiment

The primary objective of this experiment is to search for the appearance of electron neutrinos in a $\nu_\mu$ beam of about 1.5 GeV average energy through a comparison of $\nu_{\rm e}$ charged current interactions in detectors located at two different distances (127 and 885 meters) from the proton target. This can be achieved by restoring the neutrino beam line from the CERN PS and using existing experimental halls.

The detectors will measure at different distances the relative $\nu_{\rm e}/\nu_\mu$ interaction rate. With the estimated $\nu_{\rm e}$ and $\bar{\nu}_{\rm e}$ contamination in the proposed beam, and in the absence of any other phenomenon, this relative rate is about $6 \times 10^{-3}$. The occurrence of $\nu_\mu \rightarrow \nu_{\rm e}$ oscillations will be detected by measuring a different $\nu_{\rm e}/\nu_\mu$ ratio at the two locations. The comparison of the $\nu_{\rm e}/\nu_\mu$ ratio at different distances allows to reduce drastically systematic errors generated by particle misidentification, cross-section uncertainties and uncertainties in the beam composition. Compared to LSND, the proposed experiment will have

- similar L/E (1 Km/1 GeV compared to 30 m/30 MeV);
- about 10 times more events for the preferred LSND oscillation probability of $3 \cdot 10^{-3}$;
- smaller systematic errors because of the two-detector technique.

A comparison of the muon spectra from $\nu_\mu$ interactions in the near and far detectors, will also allow a search for $\nu_\mu$ disappearance.

An improvement in sensitivity to $sin^2(2\theta)$ in the $\Delta m^2 \sim 1eV^2$ region by a factor of 3 will be achieved both with respect to previous experiments (CDHS), because of the larger statistics, and also with respect to the future MiniBooNE experiment, because of the two-detector technique. If a $\nu_\mu \rightarrow \nu_{\rm e}$ is established, it would be particularly interesting to check whether, at the same $\Delta m^2$, the $\nu_\mu$ mixes also to other neutrinos.

## 2.2 Experimental layout

The experimental layout is shown in figure 2.

At the far site, the detector consists of two adjacent modules arranged to exploit fully the space available in the existing experimental hall. This configuration also helps in the assessment of the systematic errors arising from the different angular dependence of the beam components. The close detector consists of a single module, of identical design to the far detector modules, though shorter. All three detector modules (two far, one near) have the same simple structure, made of a fine grained *tracking calorimeter* that constitutes the neutrino target. The tracking calorimeter consists of a succession of layers of plastic scintillator followed by 2 mm thick iron foils. The module at the close location has 140 planes for a total mass of 104 t. The detector at the 885 m site (two modules of 320 planes each) will have a total mass of 476 t. Each scintillator plane consists of 128 bars of $3 \times 3$ $cm^2$ section, 3.84 m long, individually read-out by wave-length shifting (WLS) fibers. Given the fine granularity, the system combines tracking capabilities with good energy measurement. In the calorimeter, particle trajectories and energy loss are both sampled every $0.19X_\circ$.

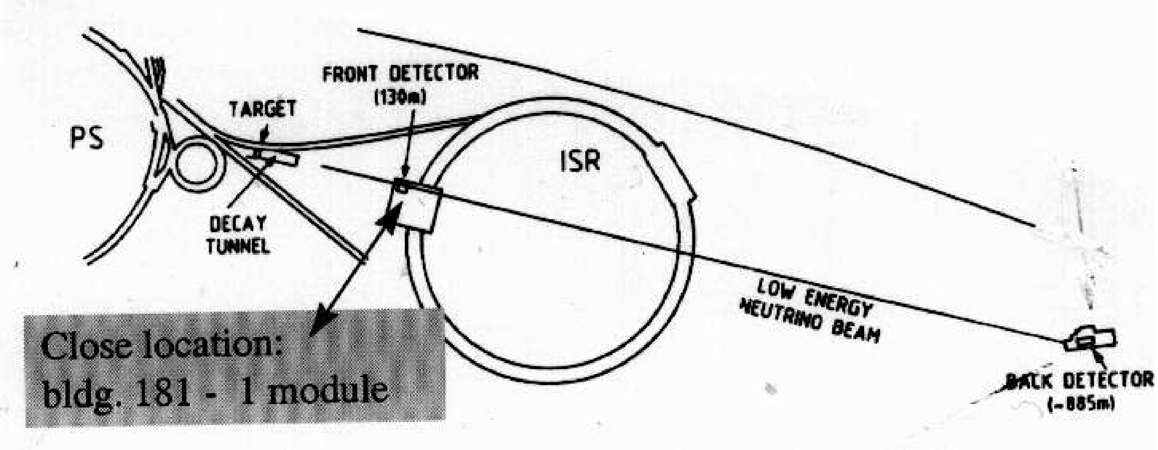

Figure 2: Layout of the experiment

The detector represents a rather innovative application of the technique of scintillators read by WLS fibers, while at the same time satisfying the requirement of a relatively short time scale for construction.

We have also studied the possibility of using liquid scintillator. Tests with cells of $3 \times 3\ cm^2$ section filled with liquid scintillator showed that the signal obtained with WLS fibers readout is even higher than in the case of plastic scintillator bars. However, the plastic scintillator performance is adequate for the needs of the experiment and this option was chosen mainly because no difficulty is anticipated during construction thanks to the extensive R&D performed on this technique by the MINOS Collaboration.

## 2.3 Sensitivity to oscillations

The neutrino reactions that will be selected are the quasi-elastic channels

$$\nu_{\rm e}\ {\rm n} \to e^{-}{\rm p} \tag{1}$$

$$\nu_{\mu}\ {\rm n} \to \mu^{-}{\rm p}. \tag{2}$$

At the energies involved in this experiment these reactions account for about 50% of all charged current interactions and can easily be identified in the proposed detector.

At the two locations, the ratio $N_e/N_\mu$ of the number of events assigned to reactions (1) and (2), respectively, will be measured. In particular, the quantity

$$\Delta_{\rm e} = \left(\frac{N_{\rm e}}{N_\mu}\right)^{\rm far} - C_{\rm e}\left(\frac{N_{\rm e}}{N_\mu}\right)^{\rm close} \tag{3}$$

will be determined, where $C_{\rm e}$ is a correction factor close to unity that takes into account the difference of the $N_e/N_\mu$ ratio at the two locations (see section 3). The error on the determination of $\Delta_{\rm e}$ will be the limiting factor in the sensitivity to neutrino oscillations. In the absence of oscillations $N_e$, the number of events experimentally assigned to reaction (1), receives contributions from genuine $\nu_{\rm e}$ ( $\bar{\nu}_{\rm e}$ ) quasi elastic interactions and from neutral current interactions where electromagnetic showers (from $\pi^{\circ}$decay) fake the $\nu_e$ quasi-elastic pattern.

Table 1: Number of electron and muon quasi-elastic events observed by this experiment under different hypotheses. The resulting values for $\Delta_\mathrm{e}$ (defined in the text) are given for the case of no oscillation and for $\Delta \mathrm{m}^2_{\mathrm{e}\mu} = 0.8\,\mathrm{eV}^2$ and $sin^2 2\theta_{e\mu} = 0.007$.

| | Close | Far | $\Delta_\mathrm{e}$ |
|---|---|---|---|
| $N_\mu$ | $3.41 \times 10^6$ | $3.48 \times 10^5$ | |
| $N_e$ $(P = 0)$ | 12140 | 1200 | $(0.0 \pm 0.8) \times 10^{-3}$ |
| $N_e$ $(0.8\,\mathrm{eV}^2$,0.007) | 12219 | 1656 | $(5.2 \pm 0.5 \pm 0.5) \times 10^{-3}$ |

Similarly $N_\mu$, the number of events experimentally assigned to reaction (2), receives contributions from genuine $\nu_\mu$ and $\bar{\nu}_\mu$ quasi elastic interactions, and neutral current events in which a charged pion fakes a muon. It should be noted that $N_\mu$ is used primarily as a normalization and therefore the important issue is not which specific channel is selected but rather that the close and far detectors select the same channels.

The expected event rates and the sensitivity of the experiment are evaluated assuming $2.5 \cdot 10^{20}$ protons on target which could be collected in a two year run (see section 3). The corresponding numbers of genuine quasi-elastic $\nu_\mu$ interactions in the close (104 t) and far (476 t) detector are $3.41 \cdot 10^6$ and $3.48 \cdot 10^5$, respectively.

Selection criteria and evaluation of efficiencies, described in section 10, allow to compute the observed numbers of events $N_\mu$ and $N_e$. They are listed in Table 1, where the corresponding values for $\Delta_\mathrm{e}$ are also given.

In the absence of oscillations, $\Delta_\mathrm{e}$ is consistent with zero. Since the close and far detectors have an identical structure, any background contribution is properly accounted for by taking the difference of the ratios, and thus a precise evaluation of each individual contribution is not required, though it is desirable that the total background be small in order to increase the sensitivity to oscillations. A value of $\Delta_\mathrm{e}$ significantly different from zero would be a clear indication for neutrino oscillations.

The sensitivity to oscillations is increased if the energy spectra of the electron in the near and far detectors are compared in addition to the total numbers of events. Should the total and differential values of $\Delta_\mathrm{e}$ be consistent with zero, then the experiment would obtain the curve shown in figure 3 as 90% C.L. limits on the oscillation probability.

In Table 1 we give an example of the results which would be obtained for $\Delta \mathrm{m}^2_{\mathrm{e}\mu} = 0.8\,\mathrm{eV}^2$ and $sin^2 2\theta_{e\mu} = 0.007$ (the corresponding mixing angle of the LSND claim). In this case the experiment would observe an excess of 456 events in the far detector and measure a value of $\Delta_\mathrm{e} = (5.2 \pm 0.5 \pm 0.5) \times 10^{-3}$, which is different from zero by more than 7 standard deviations (more than 10 standard deviations if the energy spectrum is used).

As figure 3 shows, the sensitivity in the region $\Delta \mathrm{m}^2 \sim 1\mathrm{eV}^2$ is much larger than that of previous experiments performed with a similar beam at the Brookhaven AGS and at the CERN PS. This is due to a combination of three factors: high statistics, good electron identification, and a technique based on close and far detectors for a safe control of the backgrounds.

The use of two detectors is the main reason for improvement with respect to experiments of similar statistics performed at the Brookhaven AGS (BNL 776 [8], BNL 734 [12]). In order to detect oscillation probabilities of the order of $10^{-3}$ or less, it is necessary to achieve a very good control of the background. For instance, single

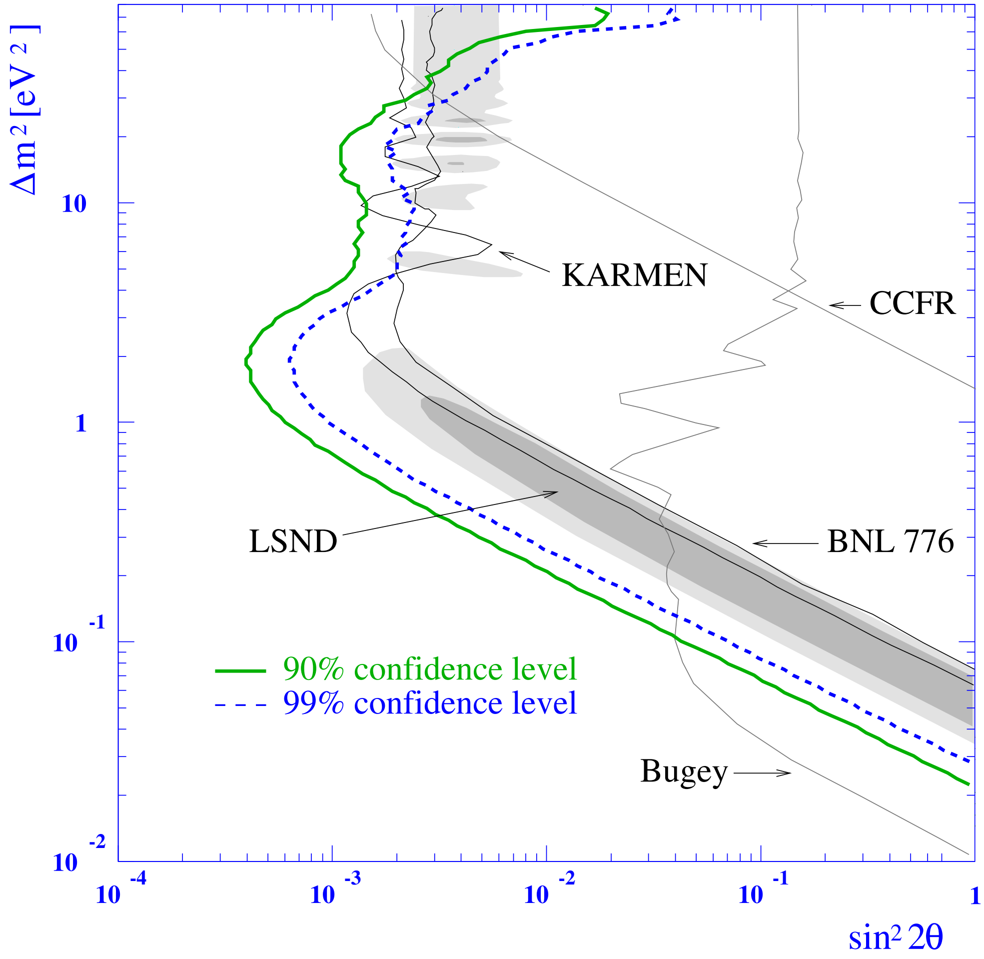

Figure 3: Sensitivity of the proposed experiment to $\nu_\mu \rightarrow \nu_e$ oscillations

$\pi^\circ$ events which could fake electron events have to be reliably suppressed by a factor of 100 or more. Only if the residual contamination is measured in a close detector can the related systematic error be neglected.

Searches for neutrino oscillation using the PS beam have been performed by the CDHS [13] and CHARM [14] collaborations, with the near/far detector technique. These experiments had much lower statistics and only limited electron identification capability, and the main results were obtained in the $\nu_\mu$ disappearance search. Interesting limits on $\nu_\mu \rightarrow \nu_\mathrm{e}$ oscillations were obtained by the BEBC experiment [15], exploiting the unmatched pattern recognition power of bubble chambers. The total statistics was however of the order of 500 $\nu_\mu$ interactions only.

In the future, the main competitor to the experiment proposed here is the MiniBooNE experiment, already mentioned previously, now in preparation at Fermilab. The detection technique is similar to that used by LSND and the neutrino energy will be in the range 0.15 to 2 GeV. The MiniBooNE experiment will use a single 770 t detector (the fiducial mass is 445 t) at 500 m from the neutrino source. Final results would be available in year 2003 [10].

The design sensitivity of MiniBooNE to $\nu_\mu \rightarrow \nu_\mathrm{e}$ oscillations is greater than ours, but our proposal benefits from the following important advantages:

- very good control of systematic errors due to the use of the two-detector technique;
- extremely fine granularity of the detector allowing very good identification of electron and muon events;
- high sensitivity to the $\nu_\mu$ disappearance search, again making use of the two-detector technique.

# 3 The neutrino beam

## 3.1 Requirements on the PS neutrino beam

Our experiment imposes the following main requirements on the CERN-PS neutrino beam:

- the integrated $\nu_\mu$ flux at the far detector must be as large as possible, as the statistical uncertainty on the number of electron events at the far detector governs the sensitivity of the $\nu_e$ appearance measurement;
- the energy spectrum must be peaked at around 1 GeV, so that L/E is well matched to the $\Delta m^2 \sim 1\ eV^2$ region we are proposing to investigate, and rapidly falling above 2.5 GeV, to reduce the $\pi^\circ$ background;
- the electron neutrino contamination $(\nu_e + \bar{\nu}_e)/(\nu_\mu + \bar{\nu}_\mu)$ should be kept at the lowest possible level.

In addition, one has also to strive to achieve the following

- for $\nu_e$ appearance: the smallest possible uncertainty in the estimate of the contamination of $\nu_e$ events $(\nu_e + \bar{\nu}_e)/(\nu_\mu + \bar{\nu}_\mu)$ expected at the far detector in the absence of oscillations. This is the dominant systematic uncertainty on this measurement whose size, with the near/far technique, is determined by the statistical error in the measurement in the near detector and by the systematic uncertainty in the ratio of the far and near contamination. This is also true in the large $\Delta m^2$ region ($\sim 10 eV^2$) where oscillations would already be detectable in the near detector.
- for $\nu_\mu$ disappearance: the smallest possible uncertainty in the estimate of the muon event rate at the far detector, and therefore, as the rate is measured in the near detector, in the estimate of the ratio of $\nu_\mu$ events in the two detectors.

Our control of systematic uncertainties benefits from the fact that, as the ratio of detector distances is only about a factor 7, the approximate shadow of the far detector is a significant fraction of the near detector. If rates and contaminations are measured in a suitably restricted area of the near detector, their values in the far detector can be estimated with only small corrections and will thus be affected by small systematic errors. In addition, the approximate independence of quasi-elastic cross sections on the neutrino energy reduces the effect of any differences in neutrino energy spectra at the two detectors.

## 3.2 The PS neutrino beam line

As a starting point we have considered the beam set-up used by the BEBC-PS180 [15] $\nu_\mu \to \nu_e$ experiment. In that experiment a 19.2 GeV/c proton beam was extracted from the PS via the transfer tunnels TT2, TT1 and TT7 and impinged on a 80 cm long, 6 mm diameter beryllium target. The latter was followed by a magnetic horn designed to optimally focus positive particles of momentum around 2 GeV/c. After focusing, the particles propagated in a decay tunnel of about 50 m length. The tunnel has a cross section of $3.5 \times 2.8\,m^2$ for the first 25 m and $5.0 \times 2.8\,m^2$ for the remaining

25 m to allow for the decay of mesons with a larger angular divergence with respect to the beam axis. The tunnel is then followed by iron shielding of 4 m thickness and by about 65 m of earth where all remaining hadrons and most of the muons were absorbed. The resulting neutrino beam at the BEBC location is doiminantly $\nu_\mu$, with a mean energy of about 1.5 GeV, with a 0.4% $\nu_e$ component of mean energy about 2.5 GeV.

This beam line can be made operational again with only limited effort. Proton beam line magnets and supplies are all recoverable. In a recent study [17] the cost was estimated to about 4.2 MSF and the time required to be about two years, overlapping scheduled PS shutdown periods. Details of these costs are given below.

A new target and horn are required due to the high radioactivity of the existing components. This opens up the possibility of redesigning the optics of the secondary (neutrino parent) beam so as to best match the aims of our experiment. On the contrary, only minor modifications to the overall geometry of the primary proton beam are foreseen.

The proton beam is to be fast extracted at 20 GeV/c in straight section SS16. The spill length is 2.1 $\mu$sec, with a fine structure consisting of 16 bunches, 25 ns long and spaced by 131 ns.

The close detector station is located in the existing pit, used by previous oscillation experiments [18],[14],[13], at a distance of 127 m from the target, while the far detector can be located in the CHARM II [19] experimental hall at about 885 m distance from the target.

## 3.3 Requirements on proton intensity

The total number of protons on target (PoT) needed to provide the integral neutrino flux for the proposed experiment is about $2.5 \cdot 10^{20}$.

A preliminary study was conducted in the PS Division [21] to establish whether the number of protons/year required by our project and by other users of PS protons matches the expected number of protons/year available from the PS in the coming years. This study concluded that the PS is capable of providing the required number of protons in about two years of operation.

PS protons originate in the proton linac (LINAC II) and are accelerated first in the Booster (PSB) and then in the PS machine. The latter operates in a supercycle which is a multiple of the 1.2 s repetition time of the booster. It consists of 12 PSB cycles of 1.2 s duration.

The maximum number of protons that can be accelerated in each PS cycle is limited by the booster to about $3.0 \cdot 10^{13}$. A much more stringent limit to the total number of protons that the PS can deliver to users comes, however, from the safety requirement that the losses of protons from the machine be kept on average below $5 \cdot 10^{11}$ p/s. As losses presently amount to about $5 - 10\%$ of the accelerated beam, the average intensity of protons circulating in the PS is limited to 5-10 $\cdot\ 10^{12}$ p/s. Among the by now completed upgrades for operation of the LHC is the injection of protons from the PSB to the PS at an energy of 1.4 GeV instead of 1 GeV, leading to a reduction of beam losses due to the lower emittance. It appears therefore reasonable to assume that it will be possible to accelerate $10 \cdot 10^{12}$ proton/s in the PS on average.

Within these constraints, about $1.8 \cdot 10^{20}$ PoT per year could be delivered by the PS to users in a year of operation of 233 days (5600 hours). Based on recent performance a 92% efficiency is assumed and an additional 20% reduction factor is applied to take into account the fact that the PS cannot permanently operate at peak intensity.

Given the requirements on PS protons in the years 2001-2003 when we propose to take data (the WA neutrino beam is no longer in operation and the proposed Gran Sasso neutrino beam will not yet have begun operation; the SPS will only need to run at limited intensity) it appears conceivable for our proposed experiment to collect a large fraction of the total protons from the PS and complete data taking within about two years.

A preliminary baseline scheme for future PS operation, at the above average intensity, has been proposed [21]. This scheme assumes that in a 14.4 s PS supercycle, three 1.2 s cycles are dedicated to fast extraction in the TT7 beam line towards the neutrino target (see fig. 4).

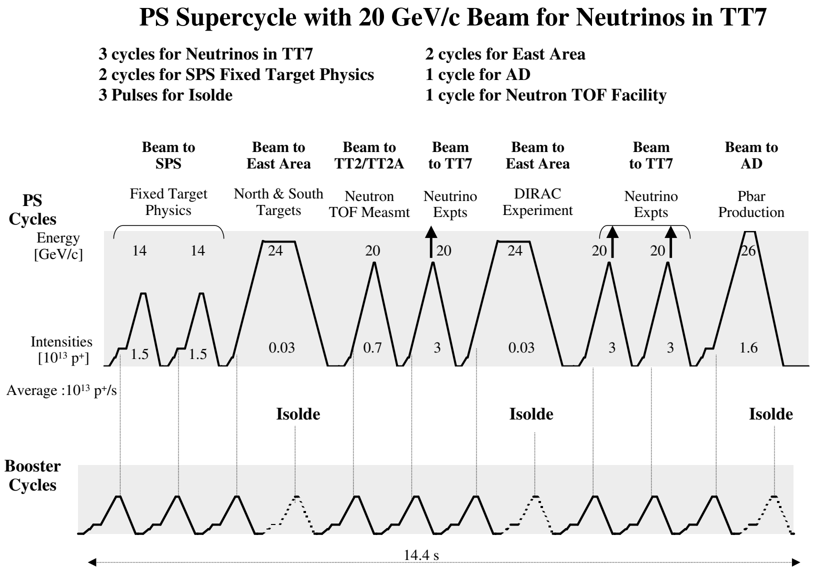

Figure 4: Baseline scheme for the PS super-cycles

Each cycle would provide $3.0 \times 10^{13}$ protons and about $8 \times 10^{19}$ protons/year can be delivered in a year of operation of 195 days (6.5 months). This is compatible with the average intensity of $10 \cdot 10^{12}$ proton/s as most PS cycles provide far lower intensities.

In addition, beam can be fast extracted towards our detector in the two PS 2.4 s cycles that provide beam to slow extraction users in the East Area. The implementation of such a shared extraction scheme has been tested and appears to be feasible. As slow extraction uses only a small fraction of the accelerated beam, most of the intensity ($2.2 \times 10^{13}$ pot/cycle) could be extracted towards the neutrino target. This would represent a 50% increase over the baseline scheme.

In any event, more than the 3 baseline cycles will certainly be available to us in the last month of operation every year, when all other PS users (except ISOLDE) are off.

Taking into account this possibility of shared extraction and the availability of additional cycles in the last month of operation of the machine, a working scheme fulfilling the requirement of about $2.5 \cdot 10^{20}$ protons on target in two years or so does appear realistic.

### 3.4 Beam simulation

For the LOI, [22] a GEANT based simulation program was developed to study the relevant features of the neutrino beam at the two detector locations. This program included the elements ( target, horn, decay tunnel etc ) of the BEBC beam set-up described in the previous section. The hadronic interactions in the beryllium target were generated by the FLUKA generator (GFLUKA) available in GEANT [23].

Since the LOI further effort has gone into these simulations. They are now being carried out using a new and more complete simulation program adapted from the one in use [20] for the design of the CERN to Gran Sasso beam. While the basic geometry of the beam (size of the target and horn hall, decay tunnel, shielding) must be kept unchanged, we are also studying in addition to the BEBC set-up a number of modified horns and targets. The results presented here are based on the original PS-180 configuration.

Fig. 5 shows the spectra predicted by this simulation for $\nu_\mu$, $\overline{\nu}_\mu$, $\nu_{\rm e}$, $\overline{\nu}_e$, at the far detector location. As a comparison the results for $\nu_\mu$ and $\nu_{\rm e}$ of the original simulation, carried out for the BEBC PS-180 experiment, are superimposed, showing that the main features of the spectra are reproduced in a similar way by the two simulations. The $\nu_\mu$ yields are consistent with the BEBC simulation, while the $\nu_{\rm e}$ contamination is higher (0.6%). That is the value already provided by our preliminary simulation at the time of the LOI and thus appears to be a more reliable estimate. The BEBC simulation was carried out 15 years ago with older and less detailed simulation programs and it was checked only roughly against a handful of $\nu_{\rm e}$ events. Differences are in any case small in the region of neutrino energies of most importance to our analysis, where the $\nu_{\rm e}$ contamination is 0.3%.

The energy distributions of the two main neutrino components are not too dissimilar at the two detector locations as can be seen in figure 6. The muon neutrino energy spectrum is harder at the far detector, but this will not introduce large differences in the number of quasi elastic events produced. Furthermore differences in the spectra are much reduced if only neutrinos hitting the central part of the near detector (at radial distance $r < 28$ cm) are considered, as shown in the dashed histogram in fig.6.

The radial profiles of the $\nu_\mu$ and $\nu_{\rm e}$ neutrino fluxes at the far and near detector are shown in fig. 7. The profiles are all rather flat over the surface of the detectors with the exception of the $\nu_\mu$ profile at the near detector that has a HWHM of about 3 m.

Though the absolute neutrino fluxes predicted by the simulation are affected by large systematic errors, the quantities relevant to our analysis are the relative fluxes $(\nu_{\rm e} + \bar{\nu}_{\rm e})/(\nu_\mu + \bar{\nu}_\mu)$ and their ratios between far and near detector. These quantities can be extablished much more reliably.

As mentioned earlier, the most relevant quantity for the $\nu_{\rm e}$ appearance search is the $\nu_{\rm e}(\bar{\nu}_{\rm e})$ contamination and its variation along the path to the two detection positions. Figure 8 shows the flux ratio $(\nu_{\rm e} + \bar{\nu}_{\rm e})/(\nu_\mu + \bar{\nu}_\mu)$ in a region of 2 m radius about the beam axis, integrated over $\nu$ energies, as a function of the distance from the target. The average contamination decreases with distance, as expected because the $\nu_\mu$ component of the beam is more forward peaked than the $\nu_{\rm e}$ component. It is of the order of 0.5% to 0.6% with no energy cut and about 0.3% to 0.4% when imposing cuts on the $\nu_{\rm e}$ energy similar to those required in the event selection (section 9). Our

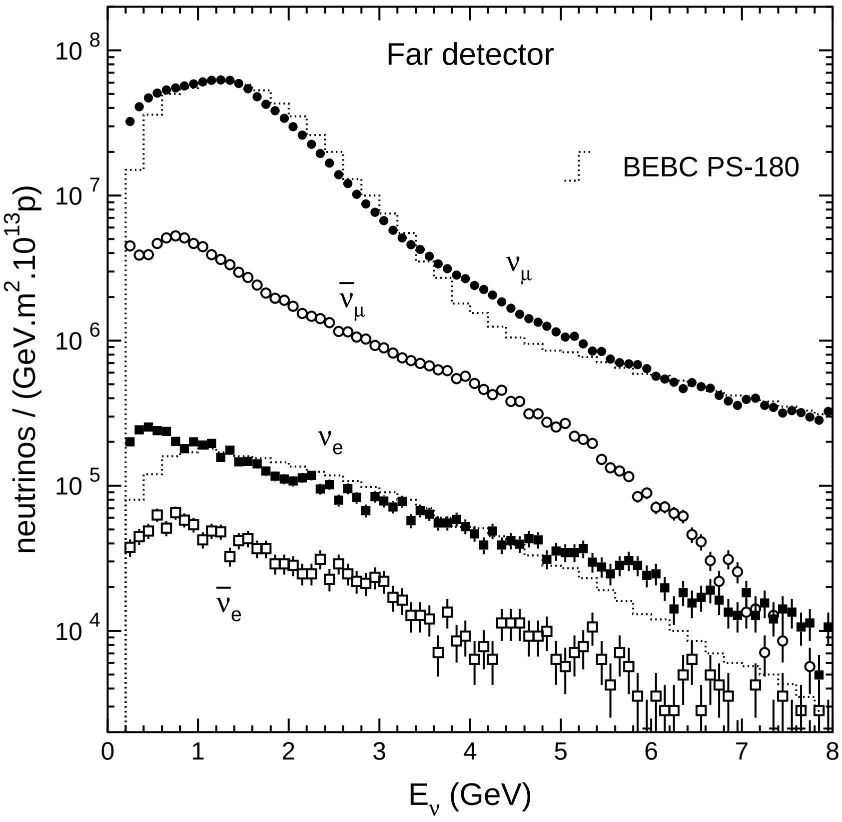

Figure 5: $\nu_\mu$ and $\nu_\mathrm{e}$ energy spectra at the position of the far detector from the current simulation (full symbols) compared with similar spectra from the simulation used for the BEBC PS-180 experiment (dotted lines). Also $\overline{\nu}_\mu$ and $\overline{\nu}_e$ are shown for the current simulation.

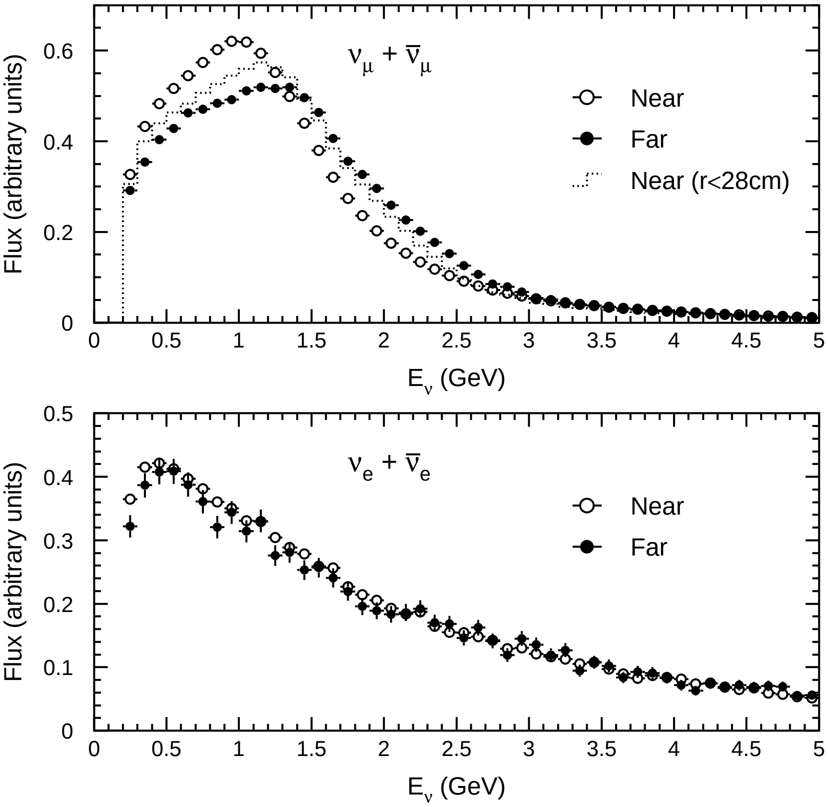

Figure 6: $\nu_\mu + \overline{\nu_\mu}$ (top) and $\nu_e + \overline{\nu_e}$ (bottom) energy spectra for the near (open circles) and far (solid circles) detectors. The dashed histogram contains only $\nu_\mu$ hitting the central part ( radial distance r< 28 cm ) of the near detector.

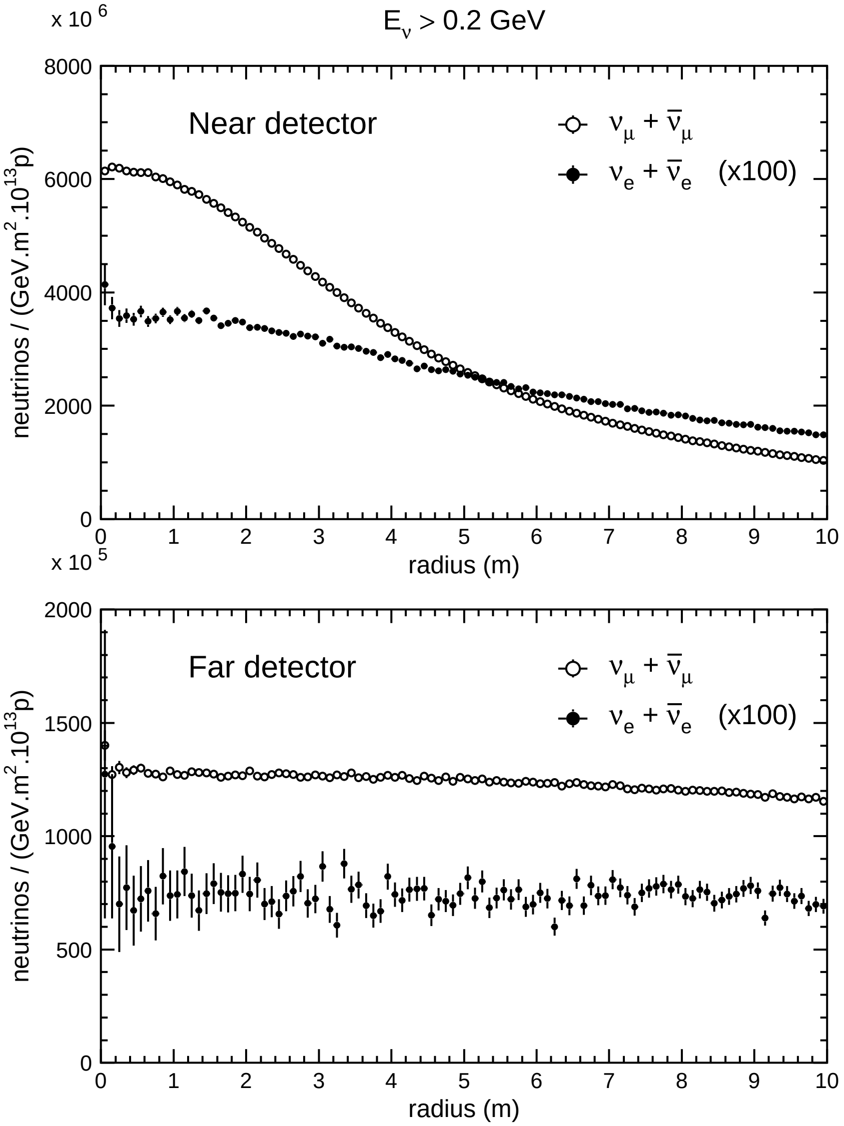

Figure 7: $\nu_\mu$(open circles) and $\nu_{\rm e}$(solid circles) fluxes as a function of radial distance from the beam axis for (a) the near and (b) the far detectors.

simulation predicts that, for energies within the selection cuts, the relative difference between the contamination at the near detector (slightly larger than 0.4%) and at the far detector ( about 0.36% ) is of the order of 13%.

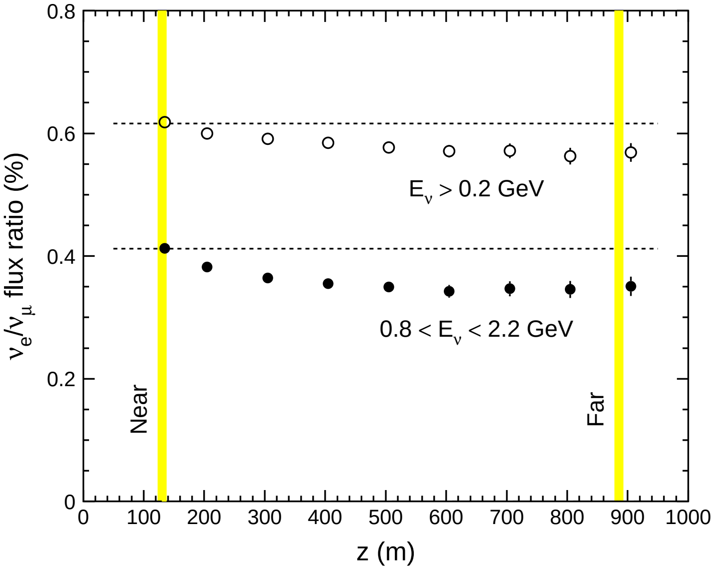

Figure 8: Flux ratio $(\nu_e + \bar{\nu}_e)/(\nu_\mu + \bar{\nu}_\mu)$ as a function of the distance from the target for all neutrino energies (above 0.2 GeV) and for the energy cuts mentioned in the text.

The contamination in the far detector can be measured with small uncertainty. Figure 9 shows the flux ratio $(\nu_e + \bar{\nu}_e)/(\nu_\mu + \bar{\nu}_\mu)$, integrated over $\nu$ energies, as a function of radius for both detector locations. A measurement of the contamination in the central part of the near detector has a small (1 to 2 % ) statistical error and a small correction with small systematic uncertainty is needed to extrapolate it at the far detector. We have adopted a conservative estimate of the total uncertainty on the contamination at the far detector of 3.5%, similar to the statistical uncertainty in the number of electron events in the far detector, the dominant factor in the final sensitivity to oscillations, as discussed in section 11.

A similar procedure has been studied to estimate the uncertainty in the estimate of $\nu_\mu$ flux in the far detectors in absence of oscillations, relevant for $\nu_\mu$ disappearance. Again a suitably restricted area of the near detector that covers the approximate shadow of the far detector should be used to keep the correction small. The energy distribution for neutrinos contained in this area is shown by the dashed line in the upper part of fig. 6 and resembles more closely the distribution in the far detector; spectral distortions are thus also greatly reduced. The uncertainty, entirely due to the systematic uncertainty in the correction, is about 3%.

While the BEBC beam provides an adequate basis for the design of the experiment, it appears possible and worthwhile in many respects to further optimize it, if our proposal is approved.

We plan to operate the beam at intensities much larger than those available to the BEBC PS180 experiment . The size of the proton beam at the target will be larger than the 6 mm diameter of the old target. The size of the beam spot for a spill of $3.0 \cdot 10^{13}$ can presently only be guessed to be of the order of 8 mm or more and will

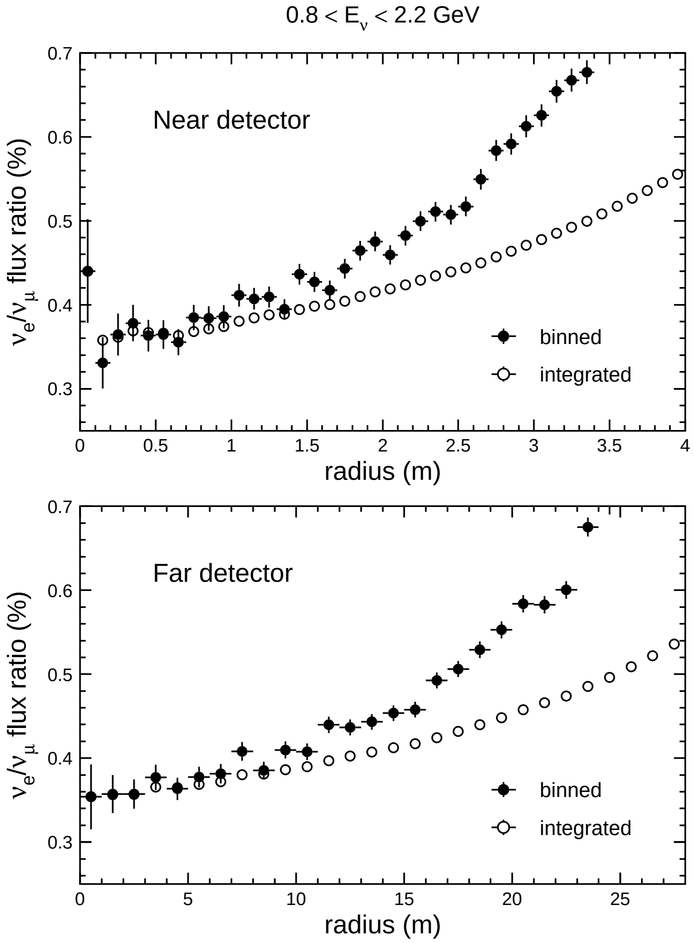

Figure 9: Flux ratio $(\nu_e + \bar{\nu}_e)/(\nu_\mu + \bar{\nu}_\mu)$, within the energy cuts mentioned in the text, as a function of the detector radius for (a) the near and (b) the far detector, both in bins of radius (solid circles) and integrated up to the given radius ( open circles)
.

have to be measured precisely in a MD period. In any event, a larger target diameter will have to be foreseen. This will have the advantage of making the target more resistent to mechanical and thermal stresses. However a larger target diameter will degrade to some extent the energy of the parent mesons and thus affect the neutrino yields and spectra. The most effective compromise has yet to be chosen.

An optimization study and a finer tuning of the production of parent mesons by proton interactions should also be carried out. Several measurements of hadron production exist at these proton energies [24] which can be used to cross check the results of the GFLUKA generator and improve the reliability of the simulation. A better match to the existing data is expected from the FLUKA program in its more recent stand-alone updates [25]. An appropriate interface exists and can be implemented with little effort.

A better horn can be designed to take into account the requirements listed above. Different horn geometries (inner conductor profile) and operational currents are being tried. Modern techniques of electron beam welding instead of bolted flanges, allowing less absorption of neutrino parents, should be used, with larger currents up to 150 kA or so. A preliminary design of an improved horn already exists [26]. These studies will continue and will aim to achieve the design of the most effective pair of target and horn elements.

## 3.5 Costs of beam reactivation

A recent study [17] estimated the cost of the reactivation of the PS neutrino beam to be about 4.2 MSF and the time required to be about 2.0 years, overlapping scheduled PS shutdown periods.

Proton beam line magnets and supplies are all recoverable. The dominant costs come from

- consolidation and lower level electronics for power converters of quads and dipoles in TT1 and TT7 (1.1 MSF);
- removal of 400 $m^3$ radioactive waste material in TT7, provisions and installations for radiation protections, access control (0.5 MSF or possibly less);
- beam line installation, vacuum chamber, joints, supports, general mechanics (0.4 MSF);
- beam monitoring instrumentation (0.4 MSF);
- civil engineering, mostly new housing needed for converters (0.5 MSF);
- a new target and horn, due to the high radioactivity of the existing components (0.4 MSF).

The remaining costs (0.9 MSF) cover several smaller items, including also some of the cost (50 KSF) of making the near experimental hall operational for our experiment (new pillars and platform).

# 4 The experimental halls

## 4.1 General layout

Fig. 10 shows the location of the neutrino beam superimposed on the CERN site plan. The neutrino beam leaving the TT7 tunnel traverses 4 m of iron followed by 65 m of earth before reaching the near detector. The near detector will be situated in the basement of building 181, at a distance of 127 m from the production target. The far detectors will be installed in building 182, at a distance of 885 m from the production target.

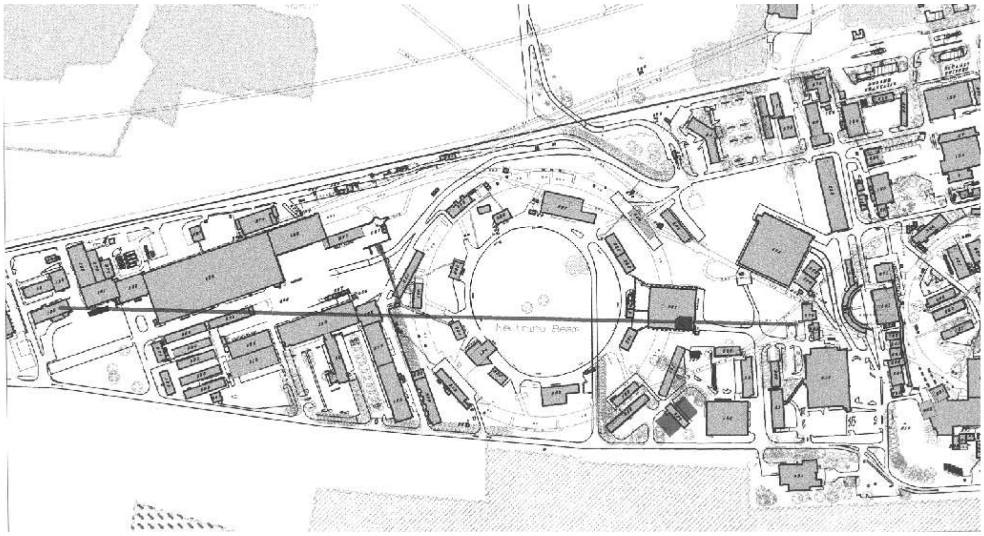

Figure 10: Location of the neutrino beam on the CERN site.

## 4.2 Hall 181

The neutrino pit in the basement of building 181 was previously used for neutrino oscillation experiments [27], [28], [29], [30]. It has an area of $17 \times 10\ m^2$ and a height of 6.26 m. These dimensions are sufficient to house the near detector. Fig. 11 depicts the location of the near detector in horizontal and vertical projections. The neutrino beam pointing at the far detector traverses the pit at a height of 2.87 m above the floor, with a slope of +1.3%. The detector will be placed horizontally. The center of the active volume will be aligned with the neutrino beam.

Hall 181 is presently housing the LHC magnet assembly facility. The space in and around the neutrino pit represents about 9% of the total floor space of the hall. Care will be taken to minimize the impact of the neutrino experiment on the LHC magnet activities. The neutrino pit is presently covered by a platform supported by concrete blocks. For the installation of the experiment, this platform will be removed. The modular design of the detector allows for a tight installation schedule of 4 months. This time includes a 6-week period necessary for refurbishing the pit (cleaning, followed by the adaptation of electricity, ventilation and cable trays). After the installation of the experiment, the area will be covered by a platform suspended from the walls of the pit. This allows for the surface to be available again for the LHC magnet activities. The near detector occupies only part of the neutrino pit as can

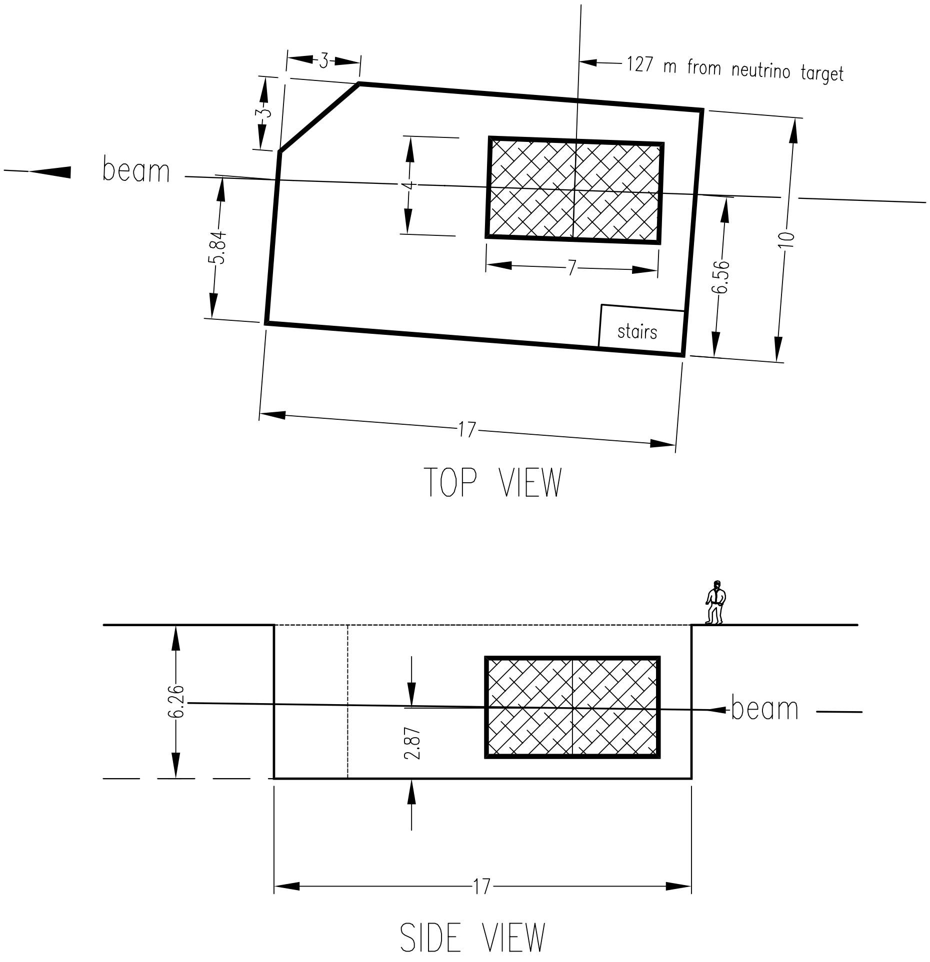

Figure 11: Top view and side view of the neutrino pit in Hall 181, showing schematically the location of the near detector.

be seen from Fig. 11. Discussions are in progress concerning the simultaneous use of the neutrino pit for the cryostat assembly of the LHC short sections. The neutrino beam operation will not induce any radioactivity in the hall, thereby excluding the obligation to use personal radiation dosimeters. The use of the magnet press, as well as the welding and machining activities in the hall are not expected to disturb the data taking of the experiment.

The detector electronics will be housed in a barrack with a surface of approximately 65 $m^2$. This barrack will be placed outside, at the Geneva-side of the hall. For cable passage to the counting room an existing gallery will be used. The main control room of the experiment will be located near the far detectors.

## 4.3 Hall 182

The two far detectors will be housed in building 182 as depicted in Fig. 12. The neutrino beam enters the hall at a horizontal angle of 22.84 degrees. The floor of the experimental area has a slope of 4.2% along the West Area neutrino beam. The detectors will be placed horizontally and their support structures will correct for the slope of the floor. The neutrino beam will be centered on one of the two far detectors.

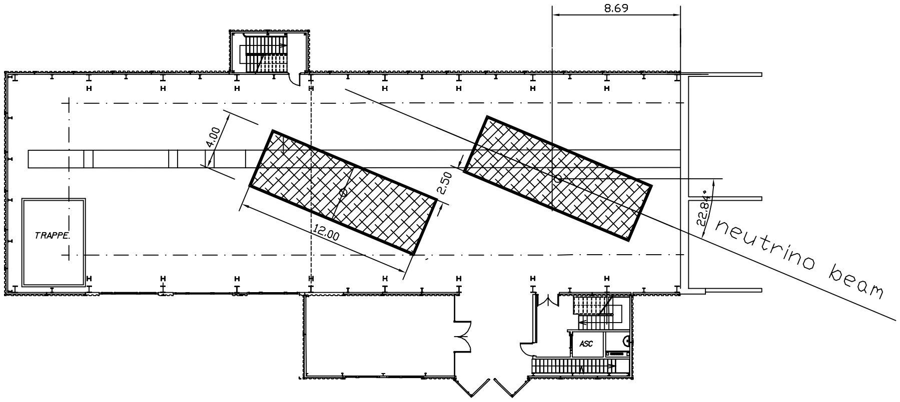

Hall 182 top view

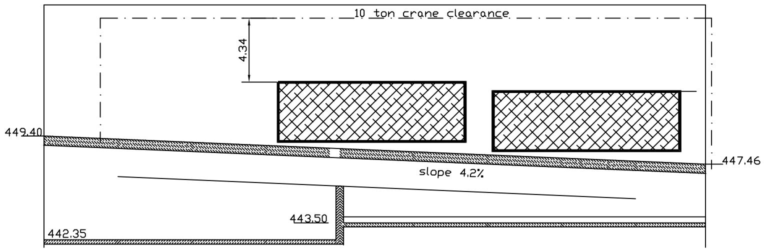

Hall 182 side view

Figure 12: Top view and side view of Hall 182, showing schematically the location of the far detectors.

To allow for a maximum height under the 10 t crane hook, this detector is placed at the east side of the hall. The second detector will be placed at a lateral distance of 6.5 m. This will reduce the systematic error on the beam composition due to the different angular acceptance spanned by the near and far detectors. The ground floor of building 182 is already well equipped to receive the electronics counting room and the main control room of the experiment. The counting room will house 25 electronics racks. These racks will be cooled by the existing ventilation system. The installation of the experiment does not interfere with any planned activities in building 182.

## 4.4 Cost estimates

Hall 181:

- Refurbishing of the neutrino pit (cleaning, painting, electricity, ventilation and fire detection) 30 kCHF;
- Platform covering the neutrino pit (50 kCHF, included in the beam costs, see section 3);
- Installation of a recuperated counting house barrack of 65 $m^2$ equipped with electricity, cooling and computer network 40 kCHF;
- Cable trench 5 kCHF.

Hall 182:

- Refurbishing of the counting room and control room (partition walls, painting, electricity, ventilation, computer network) 41 kCHF;
- Refurbishing of the experimental area (electricity, ventilation, fire detection) 44 kCHF.

# 5 The Detector

## 5.1 Introduction

The apparatus consists of three detector modules of identical structure but for the length. Each module is constructed from alternating planes of vertical and horizontal bars of scintillator read with wave length shifting (WLS) fibers. This provides a fine transverse and longitudinal granularity and allows a good measurement of the direction and energy of particles produced in neutrino interactions. In addition it provides very good discrimination between electrons and muons and also between electrons and $\pi^0$'s. Additional instrumented iron plates are located at the downstream end of the three modules to measure the energy of muons not fully contained in the calorimeter. The module at the close position consists of 140 planes, the two modules at the far position have 320 planes each. The planes are interleaved by sheets of iron of 2 *mm* thickness in order to increase the mass of the detector for neutrino interactions.

## 5.2 The scintillator bar

The basic element in the experiment is a bar of scintillator 384 *cm* long and of $3 \times 3$ $cm^2$ cross section (Fig. 13). The overall quantity of scintillator needed amounts to 400 tons and therefore precludes, on economic grounds, the use of good quality scintillator with long attenuation length. A relatively cheap solution is to use a polystyrene based scintillator doped with 1% PPO and 0.03% POPOP, extruded into bars of the required dimensions. The bar is coated with a layer of polystyrene mixed with titanium oxide which is co-extruded at the same time as the scintillator and provides light-tightness and diffusion of the light back into the scintillator.

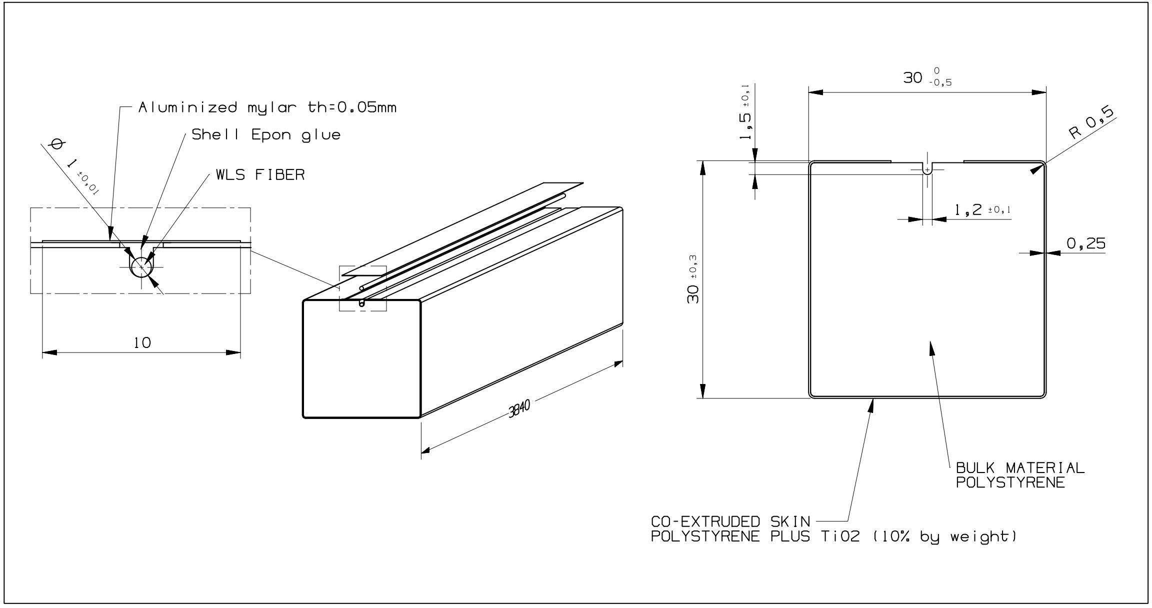

Figure 13: Views of the extruded scintillator bar and of the WLS fiber.

Because of the poor attenuation length of the scintillator the light produced in the bar is channelled to the photo-detector via green wave length shifting fibers of 1 *mm* diameter. This solution also allows the cost of the readout to be reduced by using multi-pixel photomultipliers with pixels of dimensions comparable to the fiber size. These fibers are glued to the scintillator in a groove of $1.5 \times 1.2\ mm^2$ cross section running the length of the bar and produced during the extrusion process. The wave length shifting fiber has double cladding and is aluminized at the end opposite to the photo-detector to increase the light collection.

The fiber is glued in the groove by a pneumatic driven robot which runs the length of the bar and in one pass pours a measured quantity of glue in the groove, lays the fiber in the groove, and places a 1 *cm* wide strip of aluminized mylar tape over the groove to complete the light tightness of the bar [31].

## 5.3 The Basic Unit

The basic unit consists of 32 bars glued side by side onto a 0.5 *mm* thick aluminium sheet (Fig. 14). The sheet is Ω-shaped with its two 409 *cm* long sides bent at right angles along the outer edges of the first and last bar. A second 0.5 *mm* U-shaped aluminium sheet is glued to the top of the bars.

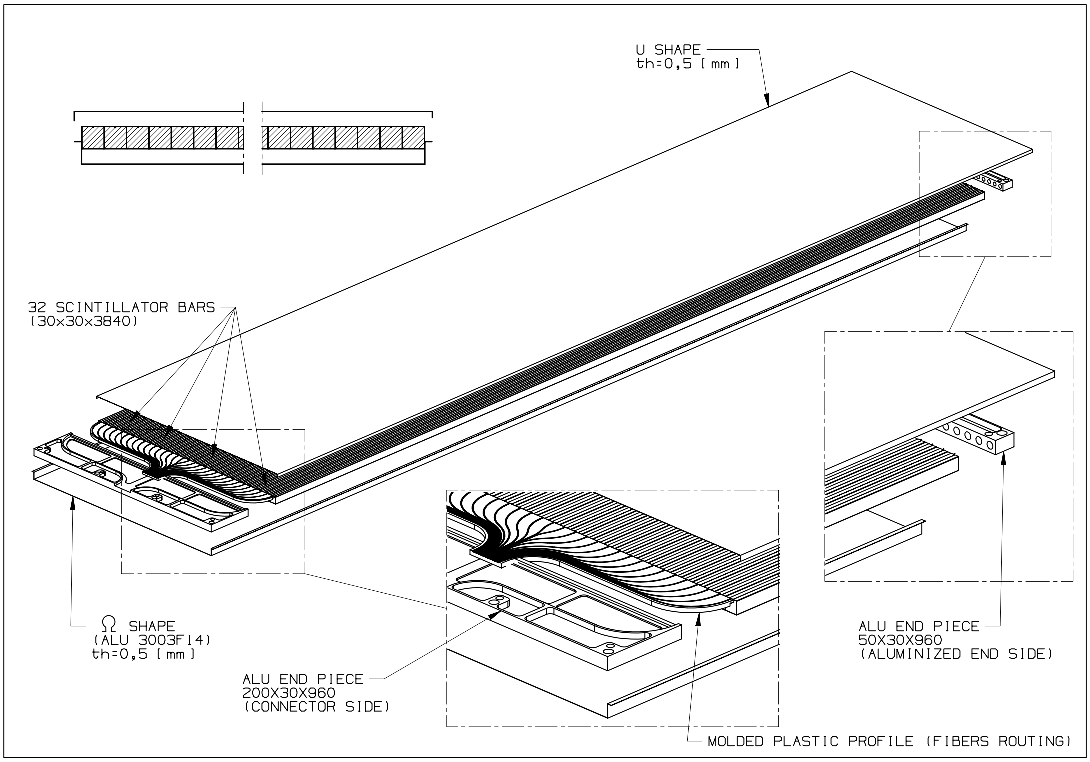

Figure 14: Exploded view of a basic unit.

The aluminium sheets extend beyond the ends of the bars, by 20 *cm* on the read out side and by 5 *cm* on the opposite side. Light aluminium end pieces are housed in these protrusions. They prevent longitudinal movement of the bars and are used to suspend the basic units from the detector overall support structure. The two aluminium sheets are crimped to each other along their length and to the two end pieces. This results in a light tight and rigid self-supporting unit, the torsional rigidity being provided by the gluing of the bars to the aluminium sheets. This design follows closely that of MINOS [31]. A moulded profile made of NORYL plastic (Fig. 15) is sandwiched between the read out end piece and the aluminium sheet closest to the fibers. It contains 32 grooves that route the fibers from the end of the bars to an optical connector placed on the edge of the basic unit. The shape of the grooves is such as to respect the minimum bending radius of the fibers of 50 *mm* below which loss of light occurs.

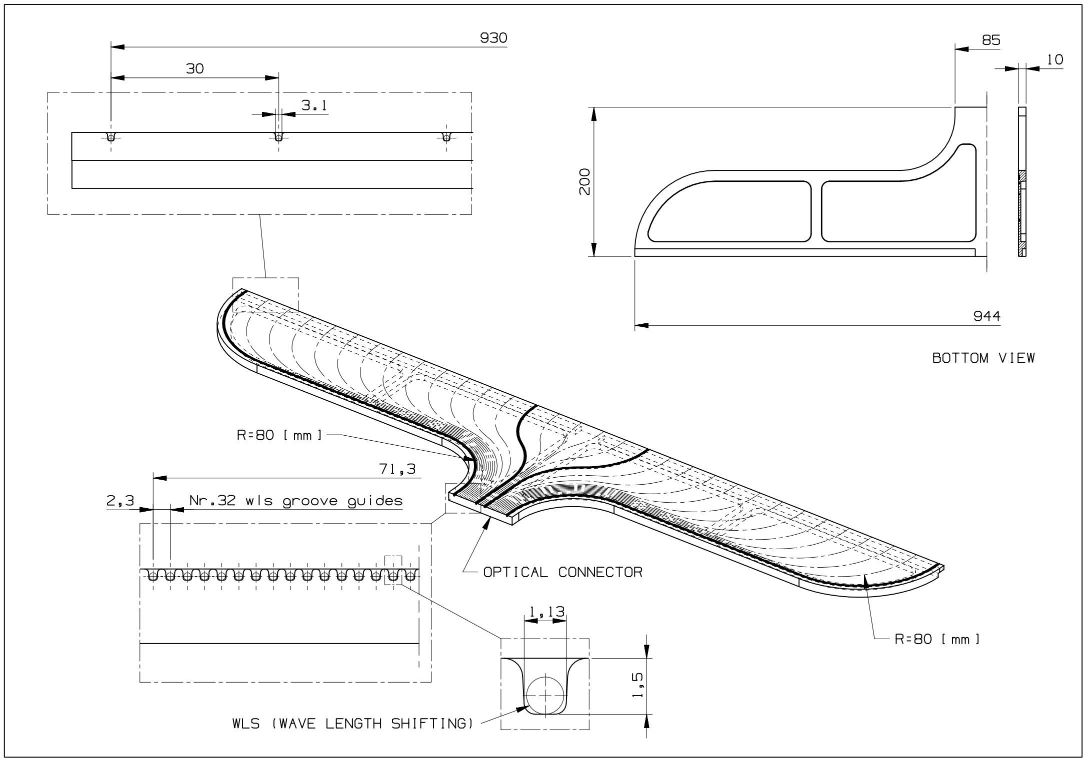

Figure 15: WLS fibers routing from the bars to the optical connector.

Thus the basic unit is self-contained from optical point of view and can be tested independently from the others. The modularity of the detector allows the production of the basic units to be shared among several centres. The basic units are robust and easily transportable from the production centres to the locations where the detector modules will be assembled. Since the units are completely independent the detector can be assembled and tested in working conditions in parallel with the production.

## 5.4 The Detector Module

A far (near) detector module consists of 320 (140) planes, each consisting of 4 basic units placed side by side (Fig. 16), corresponding to 128 bars per plane. The planes are made alternately of horizontal and vertical bars.

Two successive vertical (horizontal) planes are staggered by half a bar width in order to improve the effective granularity and to avoid systematically aligning the small cracks between the bars. Since the bars are read from one end only, the detector is made more symmetric by reading the vertical planes alternately from the top and the bottom. Similarly, the horizontal bars are read alternately from the left and right (Fig. 17). The basic units are held together by an external structure provided with positioning devices (Fig. 18). The frame structure is made of 6 (3 for the near detector) transverse arches on which longitudinal I beams are bolted. Both vertical

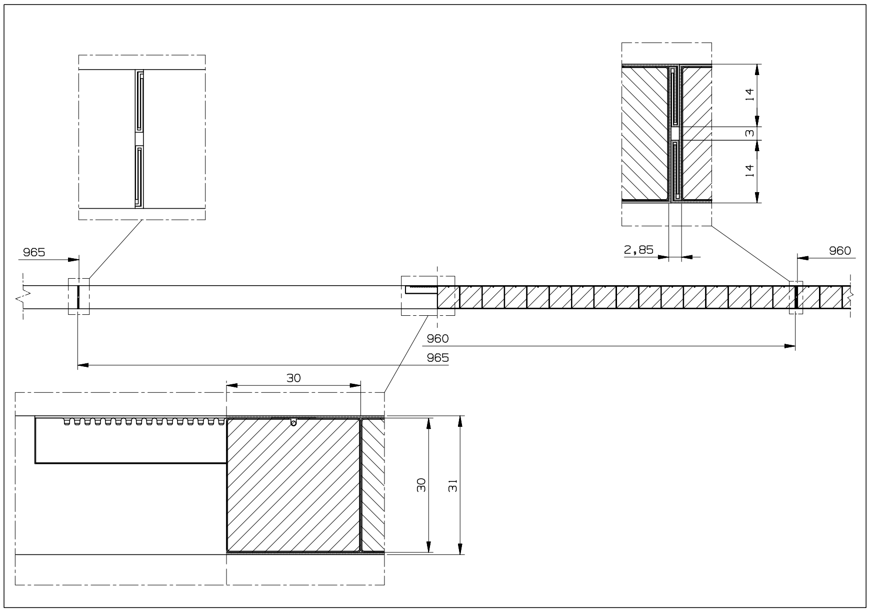

Figure 16: Assembly of a plane out of the basic units, details of the crimping of the two aluminium sheets of nearby basic units. The figure is split in two halves representing the front view and a cross section.

and horizontal units are supported from there. The vertical units are hung to avoid local buckling effects on the thin aluminium skin. The horizontal units are hung too in order to avoid the use of a support structure which would reduce the accessibility to the bottom of the detector. Vertical units are held in position by means of hollow rectangular tubes. The horizontal units are alternately suspended by means of C shaped profiles and hollow rectangular tubes, hung vertically from the I beams. At the bottom of the detector a system of rails is used in order to keep the units in position. The iron sheets are also suspended from the frame.

The photo-detectors are mounted on the detector frame. The transition between the optical connector and the photo-detectors is provided by clear fiber ribbons. The basic units of any two consecutive vertical (horizontal) planes, read from the same side and located at the same position within the plane have their optical connectors only 6 *cm* apart. The light from these two connectors will be routed to a single 64 pixel multi-anode photomultiplier by two 10 *cm* long 32 clear fiber ribbons. At the photomultiplier end these two ribbons will coalesce into a 64 fiber matrix encased in a cookie. In this solution the length of the whole readout chain, from the end of the bars to the back of the photomultiplier, is less than 40 *cm*, thus providing good accessibility and simplifying the detector assembly procedure.

## 5.5 End-system

We are studying ways of equipping the last part of the detector modules in order to obtain absorption of electromagnetic showers and an extension of muon identification and momentum measurement. A possible scheme foresees interleaving the last 14 scintillator planes of each of the three detector modules with iron plates of different thickness.

The optimisation of the thickness of the iron plates has still to be performed, since

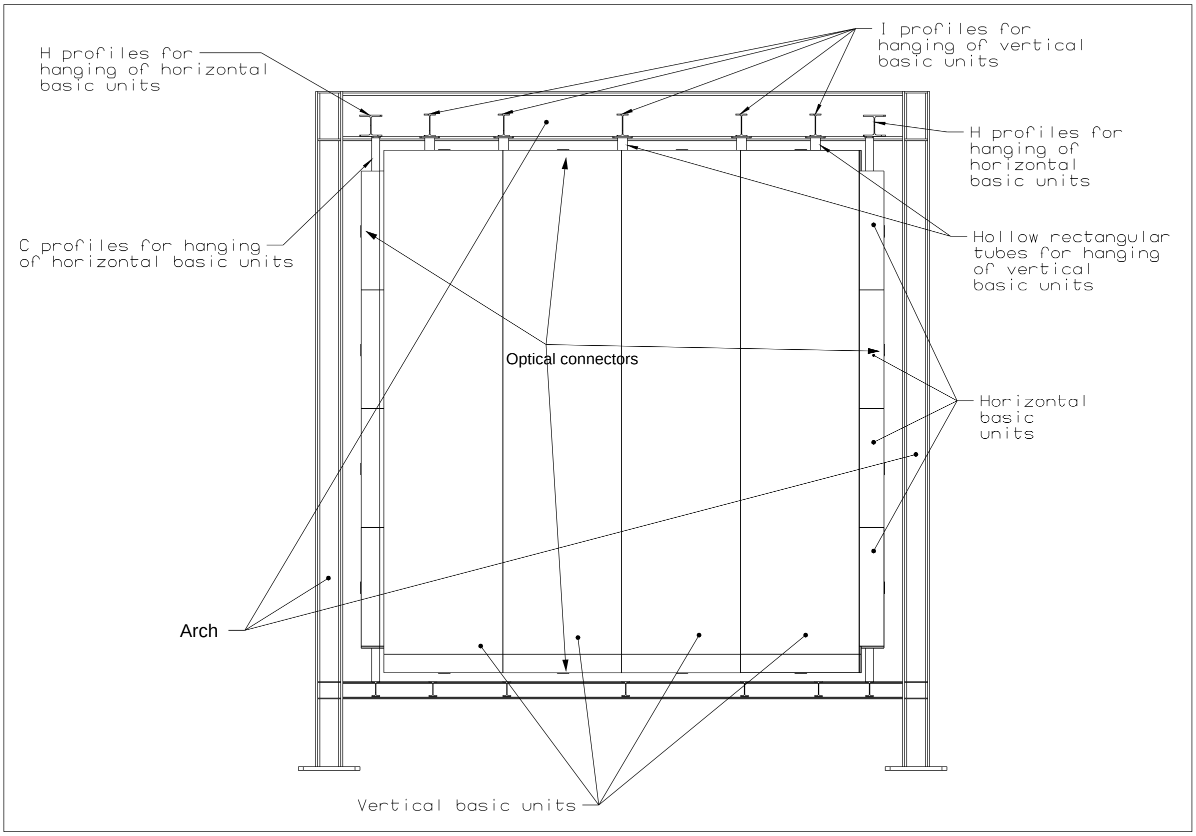

Figure 17: Front view of the assembly of the basic units of 4 consecutive planes in a detector module. The optical connectors are visible at the ends of the basic units.

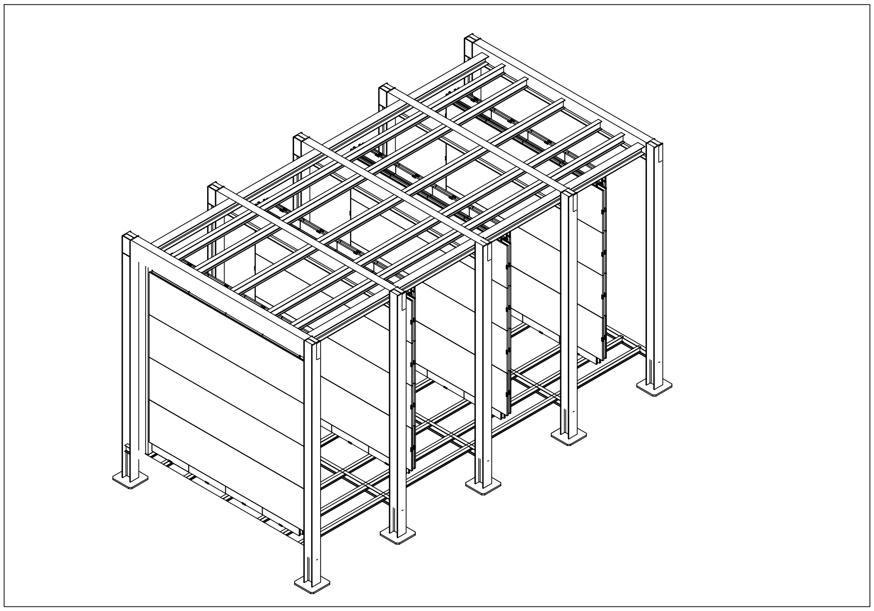

Figure 18: 3D view of the mounting of the basic units on the external frame.

it depends on the precise definition of the algorithms for electron identification. In the present design there are 7 iron plates of 2.5 *cm* thickness (= 1.42 $X_0$ each) to sample and absorb electromagnetic showers. These are followed by 7 iron plates of 15 *cm* thickness, which would allow the maximum momentum of muons stopping in the close detector to be extended to about 3 $GeV/c$. The scintillator bars with their 3 $cm^2$ cross-section allow to track and to sample the energy loss of the muon traversing the iron plates. The amount of iron for this solution is of the order of 400 tons with an estimated cost of 400 $KCHF$. Cheaper solutions for the muon momentum measurement (e.g. the use of existing magnets) are being investigated.

## 5.6 Detector performance

First tests on full size extruded scintillator bars read out with WLS fibers have been performed. The bars were produced by the company Pol.Hi.Tech [32]. They are made of extruded polystyrene and doped with 1% PPO and 0.03% POPOP. The dimensions correspond to the final design: 3 × 3 $cm^2$ cross section, 4 *m* length. For this first test the grooves for the WLS fibers and the titanium oxide coating were not produced in the extrusion process. Instead 2 × 2 $mm^2$ grooves were machined along the length of the bars and the bars were wrapped with Tyvek which yields an equivalent performance to the titanium oxide [31]. The bars were equipped with 4.2 *m* long WLS fibers of 1 *mm* diameter, also produced by Pol.Hi.Tech (POLIFI S250-100).

Measurements have been performed in various conditions (fibers on one or two faces of a bar, fibers aluminized at one end or read at both ends) to cross check the reproducibility of the results obtained by the MINOS collaboration [33]. For the readout we used photomultipliers with photon counting capabilities (Hamamatsu R1635P [34]) and HPDs (Dep PP0380C, 7 pixels [35]), both having a quantum efficiency around 10% at 520 *nm*. The properties of the bars were studied both with a $Sr^{90}$ radioactive source and with cosmic rays, in the latter using a trigger provided by a 3 scintillator telescope that selected nearly perpendicular cosmic rays. The experimental setup used is shown in figure 19. An extra length of 10 cm of WLS fiber was used to go from each end of the bar to the photo-detectors.

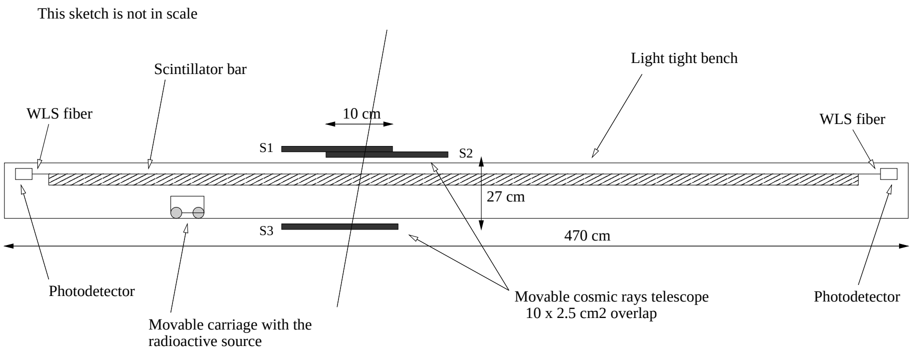

Figure 19: Experimental setup for the cosmic rays measurements and the $Sr^{90}$ measurements performed on the bars.

The response as a function of the position along the length of the bar was measured both with cosmic rays and with the radioactive source. The behaviour is essentially dominated by the attenuation of the light inside the fiber and can be fitted by the sum of two exponentials corresponding to a short and a long attenuation length:

$$f(x) = Ae^{-x/\lambda_{short}} + Be^{-x/\lambda_{long}} \tag{4}$$

We measured, with good reproducibility on all the bars, values of $\lambda_{short}$ around 40 *cm* and $\lambda_{long}$ around 350 *cm* (Fig. 20). An estimate of the uniformity of a bar can be obtained by looking at the residuals with respect to the double exponential fit: they are contained within ±10% (Fig. 21). The measurements performed with the radioactive source and with the cosmic ray trigger show similar behaviour as a function of position (Fig. 20).

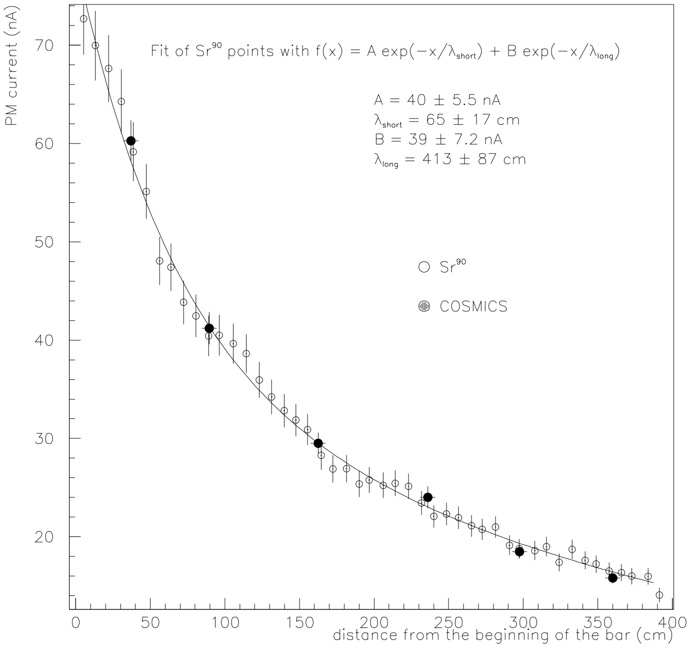

Figure 20: Response as a function of the position along the length of a bar measured with the $Sr^{90}$ source. The points obtained from measurements with the cosmic ray trigger are superimposed with an arbitrary scale.

By re-measuring the response as a function of the position after having inserted green and blue filters in between the fibers and the photo-detectors we found, by comparing the attenuation to the short and long component given by the filters, that the short attenuation length component was peaked around 500 *nm* and the long component around 520 *nm*. We measured the effective attenuation length of the light in the scintillator by using a special test bar 75 *cm* long and with a WLS fiber glued in the first 30 *cm* of the groove. By performing a fine scan with the radioactive source we could measure how much of the light produced in the scintillator in the region without the fiber was collected by the fiber after the propagation in the scintillator. A simple exponential fit to the points taken beyond the end of the WLS fiber (30 *cm*) yields an effective attenuation length of the light in the scintillator of about 8 *cm* (Fig. 22).

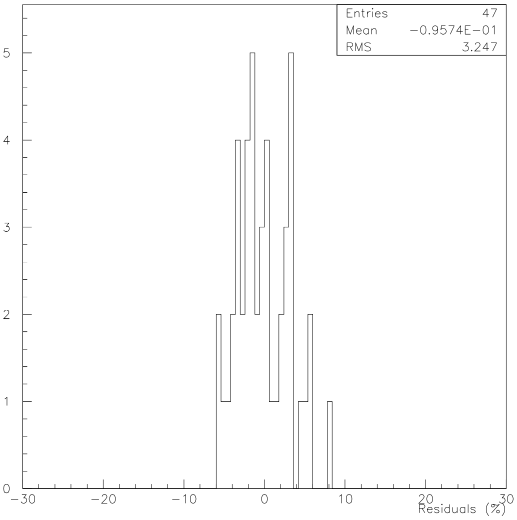

Figure 21: Residuals with respect to the double exponential fit performed on the $Sr^{90}$ measurements on a bar (see also Fig. 20).

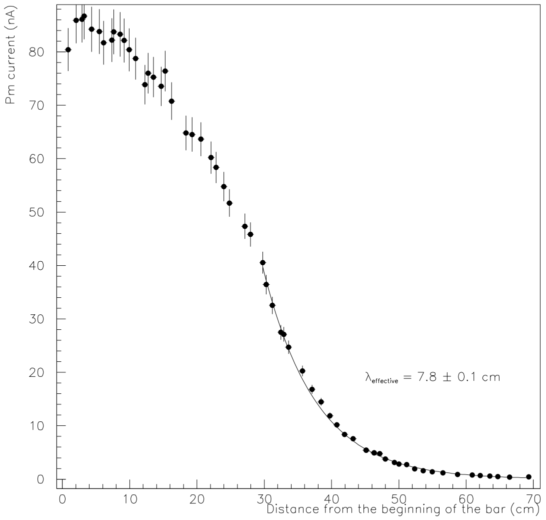

Figure 22: Effective attenuation length of the light in the scintillator measured with a bar having the WLS fiber inserted only for the first 30 $cm$.

When one end of the fiber is aluminized the fit is still valid but yields an effective $\lambda_{long}$ which is larger than in the standard case. Measurements were performed on the same bars first with one end of the fiber aluminized and then after removing the aluminization and re-machining. The data taken with one end aluminized can be fitted by reusing the function which fits the data without the aluminized end (4):

$$f(x)_{aluminized} = f(x) + R \times f(2L - x) \tag{5}$$

where L is the length of the bar and R is the reflectivity of the aluminized end, the only free parameter of the new fit (Fig. 23). We found that R was of the order of 70%, a value which can be improved by more careful aluminization.

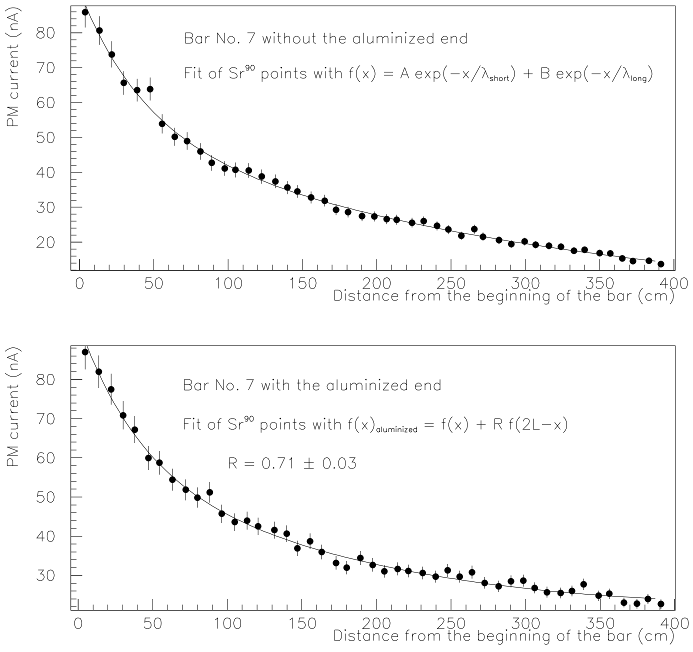

Figure 23: Measurement of the reflectivity of the aluminized end of a fiber. The reflectivity is estimated by comparing measurements performed on the same fiber with the $Sr^{90}$ source, with and without the aluminized end.

Figure 24 shows a pulse height spectrum, calibrated in number of photoelectrons, for minimum ionising particles crossing the bar perpendicularly and obtained with the cosmic ray trigger. The photo-detectors were calibrated by looking at the single electron response with a small light signal obtained from a light emitting diode.

When two fibers are glued on opposite faces of the same bar the light of each one of them is reduced by 22% because of the presence of the other fiber. The effect was measured first taking data with only one fiber and then adding the second one on the same bar. Hence having two fibers per bar does not increase the light yield by a factor 2 but only by a factor 1.56 due to this shadowing effect.

In the configuration corresponding to the final choice of the experiment (only one fiber per bar read out at only one end and the other end aluminized) the average number of photoelectrons per m.i.p. is above 10 over the whole length of the bar

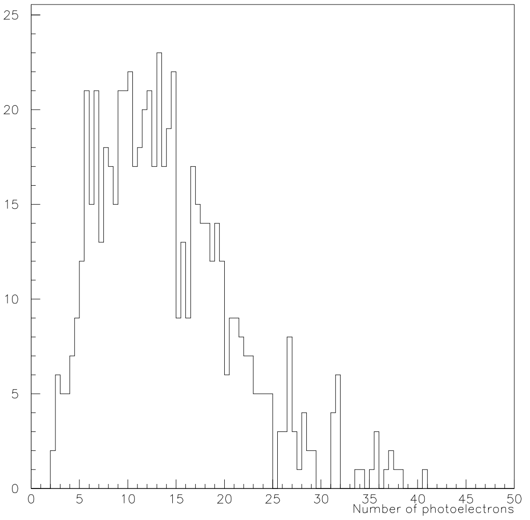

Figure 24: Calibrated pulse height spectrum for a cosmic rays run taken at at 170 *cm* on a bar without the aluminized end.

(12.7 at a distance of 360 *cm* from the photo-detector) (Fig. 25). An additional 10% reduction of the light has to be expected because of the presence of the optical connector in the final design of the basic units. The measurements of the light yield as a function of the position along the bar, when made with the cosmic ray trigger, show that the reproducibility among different bars is within 10% among the 5 bars that we tested.

In summary the tests have shown that the technique of extruded scintillator bars read out by WLS fibres is able to fulfill the requirements of the experiment in terms of light yield. The robustness of the technique is proved by the good uniformity measured within the bars and among different bars. The single side readout is feasible. The data will have to be corrected offline for the attenuation of the light in the fibers using a double exponential function.

### 5.7 Calibration of the electron energy scale

The calibration of the electron energy scale will be based on the energy response of a selected sample of cosmic muons which traverse the detector in the downstream direction.

The response of the detector to electrons will be measured in a test beam from the CERN PS. To this purpose, we plan to assemble a test calorimeter consisting of 130 consecutive basic units, corresponding to a total thickness of 15 radiation lengths.

This device will be exposed to electrons with energies between 1 and 3 GeV. We plan to perform the measurements with the test calorimeter before the end of the year 2000.

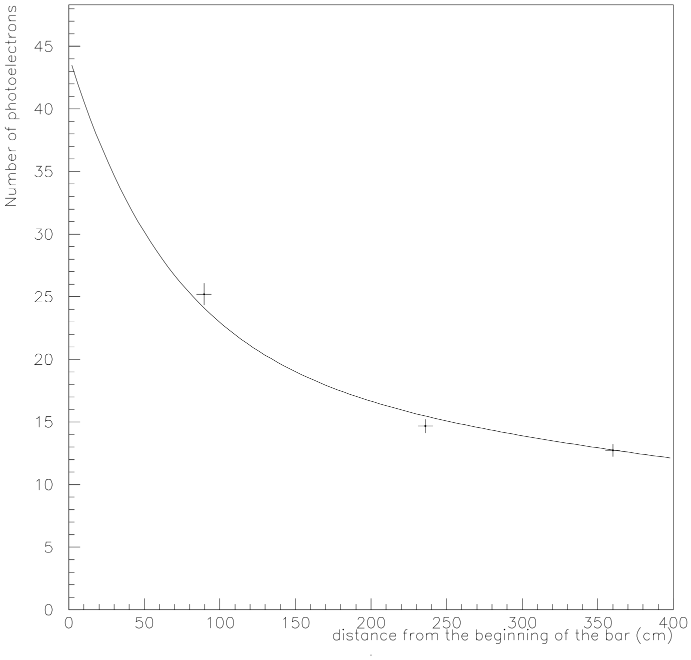

Figure 25: The average number of photoelectrons as a function of position observed in cosmic ray runs. The bar has the WLS fiber aluminized at one end. The points represent measurements taken with cosmic rays. The curve corresponds to the fit obtained from the $Sr^{90}$ data, superimposed with an arbitrary scale.

Table 2: Cost of the components of a basic unit.

| Item | Weight (Kg) | Cost (CHF) |
|---|---|---|
| 32 scintillator bars | 117 | 1107 |
| $\Omega$ sheet (0.5 mm Al) | 5.74 | 24 |
| U sheet (0.5 mm Al) | 5.53 | 23 |
| Al end piece (optical connector side) | 5.42 | 22 |
| Al end piece (aluminized end side) | 2.09 | 9 |
| Moulded NORYL plastic profile | 0.65 | 7 |
| Epoxy glue | 2 | 8 |
| Fibers ($32 \times 415cm$) | | 77.5 |
| Total | 138.43 | 1277.5 |

## 5.8 Construction time scale and costs

The estimation of the costs and the time scale for the production comes from first contacts with the companies capable of providing the extruded scintillator, the fibers and the aluminium needed for the construction of the detector.

For the production of the extruded scintillator and the WLS fibers we have received quotations of 9.46 $CHF/Kg$ and 0.58 $CHF/m$ respectively. The scintillator will be extruded with the groove and the layer of titanium oxide. The production of the scintillator is possible with commercial extrusion lines, as has already been done for the preproduction sample that we tested, after some modifications made in order to guarantee uniformity in the injection of the dopants and to perform the co-extrusion of the external layer of the bars. The price of these modifications is included in the quoted scintillator price (9.46 $CHF/Kg$).

The production scheme foresees the simultaneous use of two lines each with a profile capable of extruding two bars at the same time. This scheme will allow a single company to produce about 400 tons of scintillator on a time scale of 10 months. An additional 4 months are needed for the setting-up of the lines. The production of the fibers can also be completed in one year.

The evaluation of the total cost follows easily from the cost of the basic units. A basic unit costs about 1277 $CHF$ (table 2) and has a total weight of 138 $Kg$. The weight corresponding to the active volume is 186 $Kg$ (split among 117 $Kg$ of scintillator, 11 $Kg$ of aluminium sheets and 58 Kg of iron sheets), providing a total detector mass of 581 tons. The total price of the materials needed for the construction of the detector is hence 4.0 $MCHF$.

The external frame is made of 25 tons of iron profiles used for the I beams and the arches. The price of the profiles is estimated to be 12 $CHF/Kg$. The weight of suspension profiles of the vertical and horizontal units is about 30 tons. The unit price in this case is lower (8 $CHF/Kg$) because of the smaller amount of machining necessary. The cost of the frame is then 0.54 $MCHF$. Table 3 summarises the total cost of the detector.

The assembly of the detector proceeds in three steps:

- preparation of the bars with the WLS fibers;
- construction of the basic units;

Table 3: Calorimeter material costs.

| Item | Quantity | Unitary cost | Cost (MCHF) |
|---|---|---|---|
| Basic units | $4 \times (140 + 320 \times 2)$ | 1277.5 CHF | 4.0 |
| Frame (I beams and arches) | 25 tons | 12 CHF/Kg | 0.3 |
| Frame (suspension profiles) | 30 tons | 8 CHF/Kg | 0.24 |
| Clear fibers ribbons and connectors | | | 0.02 |
| Iron sheets | 181 tons | 1CHF/Kg | 0.18 |
| Total | | | 4.74 |

- installation of the basic units in the detector modules plus cabling.

We estimate that the first and second step have to be carried out in parallel in 4 production sites. Each site will need a team of 6 people for one year. The production sites will receive the scintillator bars and the fibers, the precut aluminium sheets, the aluminium end pieces, in their final shape, and the moulded plastic profiles from industry.

In each the site there will be a production chain for the preparation of the scintillator bars by gluing the fibers by means of the robot and for the construction of the basic units by shaping, gluing and crimping the U and $\Omega$ aluminium sheets with appropriate tools. The attenuation length of each bar will also be measured with a radioactive source by an automatic system present in the production chain.

For the assembly of a basic unit the relevant operations to be performed are the following:

1. positioning of the end pieces and the moulded plastic profile inside the aluminium sheet
2. application of the glue in strips along the length of the bar
3. insertion of the scintillator bars
4. routing of the fibers
5. application of the glue over the bars
6. closure of the box with the top aluminium sheet
7. crimping of the sides of the aluminium sheets and crimping of the sheets to the end pieces
8. hardening of the glue
9. test of the unit

In this scheme each site will be able to produce 4 basic units per day. The total production can be accomplished by the 4 sites in 200 working days. The assembly of the basic units can proceed in parallel with the production of the scintillator. The basic units can be delivered to CERN immediately for insertion in the supporting frames and connection to the electronics.

The three processes of the production of the raw materials, the assembly of the basic units and the construction of the detector can hence proceed in parallel, with a small delay relative each other. They each have a time scale of about one year.

# 6 The photodetectors

## 6.1 Description

A suitable position sensitive photodetector for the fibre read-out should fulfill the requirements of good linearity over the whole dynamic range, good channel to channel uniformity, and good quantum efficiency. Additional important issues are a low cost per channel and a production capability that should match our budget and time schedule constraints. Our baseline choice is the multi-anode photomultiplier (MAPMT) because of the ease of procurement and the relatively low cost of such devices which are widely used in similar applications [36, 37, 38, 39, 40]. The cost per channel and the superior channel to channel gain uniformity with respect to other MAPMT's have driven the selection of the R5900-00-M64, manufactured by Hamamatsu [34], as the baseline choice for our detector. We are also considering the possibility of using HPD-type or EBCCD tubes.

The M64 photocathode area is $18.1 \times 18.1\,\mathrm{mm}^2$ and the 64 $2 \times 2\,\mathrm{mm}^2$ anode pixels are arranged in a square anode matrix, with 0.3 mm space between each pixel. The dynode structure is of the metal channel plate type developed by Hamamatsu, which allows for a very compact design. Each dynode stage is made of a thin metallic plate micro-engraved with the dynode profile. The metallic plates are stacked with a separation of about 1 mm to obtain the multiplier configuration. The tube is housed in a $28 \times 28\,\mathrm{mm}^2$ square package, 50 mm deep, including the output pins. The window is an $800\,\mu$m thick borosilicate glass, with a bi-alkali photocathode. The quantum efficiency at 520 nm is about 10 %.

The M64 can be operated at a maximum voltage of 1000 V, corresponding to a nominal gain of $3 \times 10^6$. At 800 V the nominal gain is $3 \times 10^5$. The relatively low supply voltage is one of the main advantages of this tube with respect to other tubes. The need for less than 1000 V simplifies the design of the power supply system in terms of cost and quality of the electronic components and cables.

## 6.2 Uniformity and crosstalk

One of the major concerns for our application is the non uniformity of the M64 response from pixel to pixel. The dynode to dynode collection efficiency is sensitive to the spatial non uniformity given by the dynode structure along the amplification path. Most of this effect ends up in a gain variation from pixel to pixel and within the pixel surface. To a much smaller extent, limited to the first dynode collection efficiency, this effect has to be taken into account as an effective reduction of the detection efficiency. In this respect a large improvement has been achieved by the producer with respect to the early generations of MAPMT. The focusing electrodes dimensions and position have been optimised in order to improve the collection efficiency, while the photocathode resistivity has been decreased by improving the electrical contact between the photocathode and the metal package. According to the producer specifications the tubes are guaranteed to have a pixel to pixel variation such that the ratio of the responses of the highest and lowest pixels does not exceed 3. For the tube used in our tests, the distribution of the relative responses, normalised to the pixel with the highest response, had a mean value of 0.78, with an r.m.s. of 0.1. The minimum pixel response was 54% of the maximum pixel response, well within the producer specifications. We have checked that the pixel to pixel non uniformity does not change significantly with the operating voltage. It is also expected to be stable along the tube life time. Figure 26 shows the pixel responses to a 1 mm illuminating fibre scanning along three nearby pixels in steps of 250 $\mu$m. The variation of the response within the same pixel is typically within 15% when moving the axis of a fibre in a window of 1.5 mm around the pixel centre. The crosstalk depends smoothly on the fibre position and it is less than a few percent when the fibre is positioned in the centre of the pixel. When the fibre approaches the pixel edges the crosstalk is dominated by the optical crosstalk. In the test setup the distance of the scanning fibre from the photocathode was about 1 mm. No precision positioning of the fibre within the pixel is required. This is true also if the fibre diameter is increased to 1.2 mm. The effects of both the inter-pixel and intra-pixel uniformity variations will be taken into account by the long term calibration. The use of a simple cookie for the coupling of the fibres to the photocathode window will reduce the optical crosstalk to the few percent level, comparable to the electronic crosstalk.

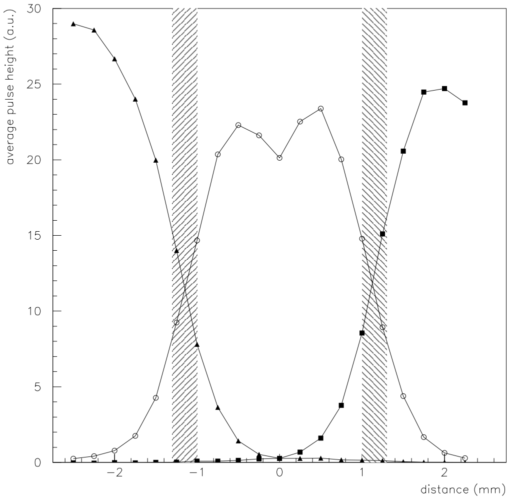

Figure 26: Responses of three nearby pixels to a 1 mm diameter fibre scanning the M64 photocathode surface in steps of 250 $\mu$m.

The detector test results indicate that the average signal expected for a minimum ionizing particle at the centre of the detector is about 17 photoelectrons (p.e.). Figure 27 shows the M64 response to two fixed amplitude pulses of a blue LED. The pulses have been calibrated to give 18 and 36 p.e. on average, which correspond to the signals expected from one and two minimum ionizing particles crossing the centre of a scintillator bar. The simulation shows that the energy deposited in one cell of the calorimeter for the highest density showers does not exceed the equivalent of about 5-6 minimum ionising particles. Our present evaluation of the dynamic range is conservatively set to 200 p.e., to take into account the fibre attenuation length effect and the MAPMT uniformity variation. Assuming a pulse width of 10 ns, the MAPMT should be operated at a gain lower than $2 \cdot 10^5$, in order to remain within the conservative single channel linearity limit (0.6 mA at 5% linearity drop) over the whole dynamic range. To avoid the saturation of the digitizing electronics, we may have to run the tube at a lower gain. This might require the use of an 8 stage M64 tube in order not to compromise the tube linearity and the detection efficiency with

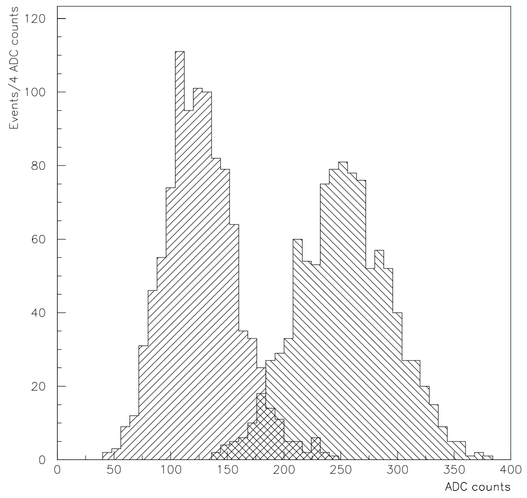

Figure 27: Responses of the M64 to two LED pulses of amplitude corresponding to the pulse height expected for one and two minimum ionizing particles.

a too low inter-dynode voltage. Gains as low as $3 \cdot 10^4$ can be obtained at a nominal HV of 720 V for an 8 stages M64 tube and a tapered (3:2:2:1...1:2:5) voltage divider. Other options are possible, including the attenuation of the signals of a 12 stage tube. The best solution which optimises detection efficiency and design simplicity will be chosen based on the results of ongoing tests.

## 6.3 High voltage system

The present design of the high voltage supply is based on a widely used system produced by CAEN [41]. It is a highly modular system, the SY527, consisting of a crate (mainframe) that can house HV generator and distribution boards of different kinds. In our design, a single HV generator board provides high voltages to 9 distribution boards which fan out the high voltage to as many as 24 output channels. The distribution boards allow high voltage regulation and control on each output channel. The resolution is 0.2 V and the maximum current is 0.5 mA at 2.5 kV. We need 280 HV channels in the near detector location and 640 HV channels each for the two far detector modules. This corresponds to 10 mainframes, 10 HV generator boards and 66 distribution boards.

We are currently investigating with the producer the possibility of using a new system, SY1527, recently made available on the market, which would allow a more compact design, reducing the number of crates and boards needed.

# 7 Readout electronics

## 7.1 Description

The role of the electronic readout chain is to record the pulseheight of signals coming from the multichannel photodetectors. The expected average event rate in the near detector is 2 events per burst of 2.1 $\mu$s duration. Of these, about one event is expected to be a neutrino interaction in the detector, and one event a through-going muon originating in an upstream interaction. We will use the start-of-burst as trigger, integrating the signals during the whole burst duration.

The 2.1 $\mu$s burst has the 50 MHz RF substructure superimposed on it. A time-stamping hardware will be used to assign each event to its RF bucket: this means that we need a timing resolution of better than 20 *ns*. The time-stamp will help in identifying possible pile-up regions in the detector.

To match the short time schedule of the construction, the low cost requirement and the relatively high number of channels to be read out ($\approx 10^5$), we will use well known and almost standard VLSI front-end electronics with a multiplexing scheme [42].

## 7.2 Choice of the front-end chip

The output signal from a multi-anode PM at standard voltage values is about $10^5$ $e^-$/p.e.; as it has already been pointed out in the previous section, we expect both from laboratory tests and MonteCarlo simulations that fixing the dynamic range at 200 p.e. gives us a comfortable margin.

These parameters will be used to choose the most suitable front-end VLSI chip. A careful compromise between photomultiplier gain and signal attenuation will allow us to match a frontend-chip to the multi-anode PM.

It should be noted that this approach is perfectly suitable also to an HPD-type tube. Its core is a silicon detector, whose signal is 3000 $e^-$/p.e., matching perfectly the characteristics of many very low noise preamplifiers [43].

A large choice of dynamic range, shaping time and noise performance is available in the list of ready-to-order VLSI preamplifier chips of the Viking family from IDEas (Norway). Some of the available chips and their characteristics are listed in their catalogue [44].

The VA (Viking) chips can host up to 128 channels with preamplifier, shaper, sample-and-hold and a multiplexer. Many chips can be daisy-chained to increase the number of channels multiplexed to 1 ADC via a single analog output. The hold signal will be sent in parallel to all the VA chips after the end-of-burst.

The VA can be complemented with the TA chip, which is a discriminator array with its own fast (75 *ns*) shaper and adjustable threshold. The chip hosts one discriminator per channel. Several channels are OR-ed to a single output; the average shower dimension allows us to OR channels in groups of 32. These discriminator signals will be used for time-stamping. The expected timing resolution is of the order of 10 ns. The output signals from the OR-ed discriminator groups will be sent to multi-hit TDCs. Figure 28 illustrates the combined use of VA and TA chips.

Good candidate chips for our readout chain are the VA_hdr family with high dynamic range for the multi-anode PM and the VA_rich for HPD-type readout. All these chips have a very low noise level, of the order of a few hundred electrons.

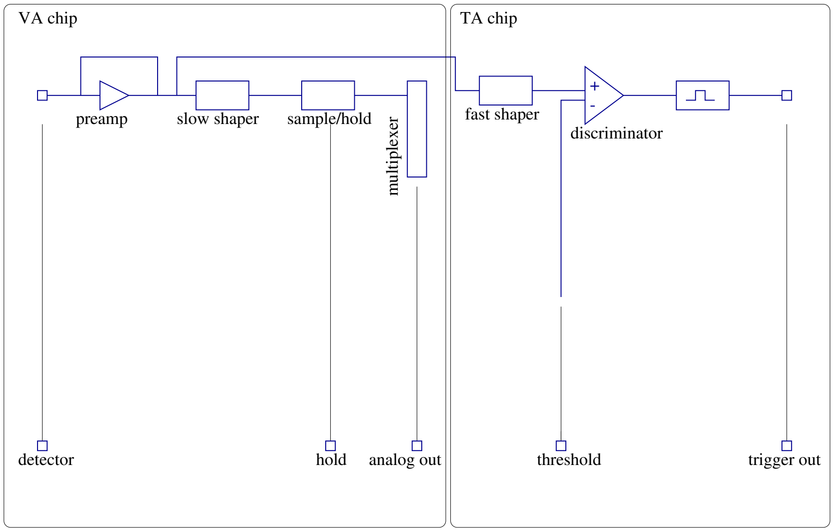

Figure 28: The VA+TA concept

VA and TA functionalities will be combined in a single chip to reduce the production cost. We do not expect that this will be a lengthy process, because a similar combination has already successfully been made for the VA2 chip, for which a VA+TA version is presently in IDEas' catalogue.

## 7.3 Electronic boards and VME modules

Figure 29 sketches the global readout structure.

The VA chips will be hosted on a front-end board. The boards will collect signals from 128 channels. Sockets will be provided on the boards for the photodetectors. The VA chips will be wire-bonded near the sockets and daisy chained.

One interface board will daisy-chain front-end boards for a total of up to 1024 channels which will be multiplexed to 1 ADC in a VME crate. The multiplexing clock will be 1MHz, so that the readout time will be limited to 1ms. Additionally, the interface board will provide the control signals and the required power supply to the front-end boards, and will drive the analog signals over large distances.

A ready-to-use solution for VA readout is a dual 12-bit ADC VME module from CAEN, which is accompanied by a sequencer VME module to synchronise VA and ADC operations. The discriminator signals provided for time-stamping will be driven by the interface board to multi-hit TDCs also housed in a VME crate.

For ease of distribution of the control signals from the sequencer and of the power supplies, a motherboard connecting 4 interface boards will be provided.

A total of 9 low-voltage modules will supply power to the readout electronics. They will be housed in slots left free in the power supply crates already described and costed for the photo-detectors.

## 7.4 Cost and time estimates

Based on budgetary quotations provided by CAEN and IDEas, we estimate the cost per channel of the described readout system to less than 10 CHF/channel. The time

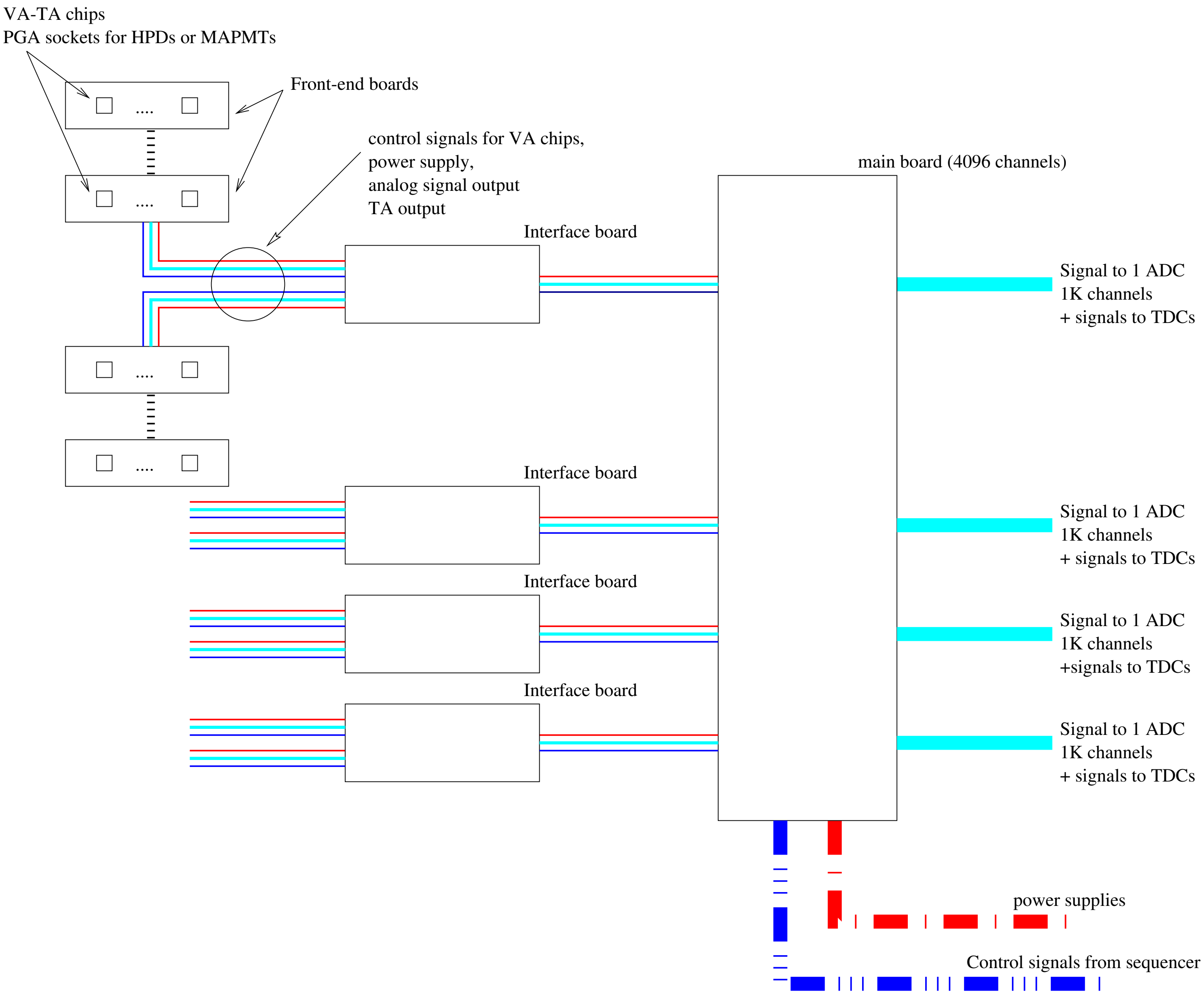

Figure 29: Readout chain structure

needed for the production has been estimated to be of the order of 6 months, and it is driven by the VLSI customisation and by the front-end board production.

A breakdown of all the costs is reported in table 7.4.

Table 4: Costs of the readout hardware

| Item | units | unit price (CHF) | price (KCHF) |
|---|---|---|---|
| 128-channel FE board | 780 | 450 | 351.0 |
| interface board | 98 | 500 | 49.0 |
| motherboard | 25 | 500 | 12.5 |
| dual ADC VME module | 49 | 4200 | 205.8 |
| sequencer module | 3 | 3200 | 9.6 |
| 128-channel TDC | 25 | 10000 | 250.0 |
| A516 8-ch +/- 12V module | 9 | 3900 | 35.1 |
| cables and connectors | | | 20.0 |
| TOTAL | | | 933.0 |

# 8 DAQ

## 8.1 Introduction

The Data Acquisition System (DAQ) will read out the digitised signals from the ADCs and the TDCs. The DAQ will also take care of several operations, including the storage in the proper sequence and format of all the data, the calibration of the detector and of the electronic readout chain, and the overall synchronisation of the readout processes.

During the burst no real trigger will be used. Signals from all photo-detectors will be integrated during the whole burst and subsequently digitised and read out. The TA chips will give a timestamp to each signal in order to identify different events by timing.

Since we want to perform a calibration with cosmics during the out-of-burst time, implementing a simple trigger is unavoidable. The cosmic ray trigger will be realized using the TA chips as auto-trigger devices.

## 8.2 Readout crates and Data Volumes

An overview of the readout configuration is shown in figure 30 .

The readout electronics configuration implies that at least 2 VME crates will be needed to house the ADC boards and the TDCs. Each VME crate will be connected to a dual-CPU readout PC via a VME-PCI interface.

The data size from the ADCs is $\approx$ 40 kWords and 17.5 kWords for the far and close detector respectively, independent of the event type. The amount of data from the TDCs is variable but we can assume that it will not exceed 1 kWords. All the data words will be 4 bytes long.

Present tests of VME-PCI links show that the bandwidth in block transfer mode exceeds 10 MBytes/s; conservatively assuming that this will be our data rate, a group of 20 ADCs (the configuration foreseen for the biggest detector block) will be read out in $\approx$ 16 ms. In comparison, the readout of the VME crate housing the TDC modules is estimated to take a much smaller amount of time, estimated to be less than 1 ms.

During the readout a data stamping key will be added to all hardware units. Associating a unique key to the data will help to unequivocally identify event blocks. Should an unforeseen error happen, an event supervising process will be able to catch it and report it.

The readout PCs will transfer their data in parallel to a dispatcher PC through ethernet links. The bandwidth of fast-ethernet (100 Mbit/s) switches ensures that the data from the whole experiment ($\approx$ 400 kBytes) will be transferred in $\approx$ 16 ms, which is comparable to the time needed to read the data from the VME modules. A zero-suppression may be safely applied at a later stage, freeing enough computing power on the DAQ-PCs for the calibration with cosmics.

## 8.3 Calibration

### 8.3.1 Electronics calibration

The calibration of the electronic chain will be performed using a special operating mode of the sequencer which allows pulsing of the VA chips with a controlled pulse charge and duration.

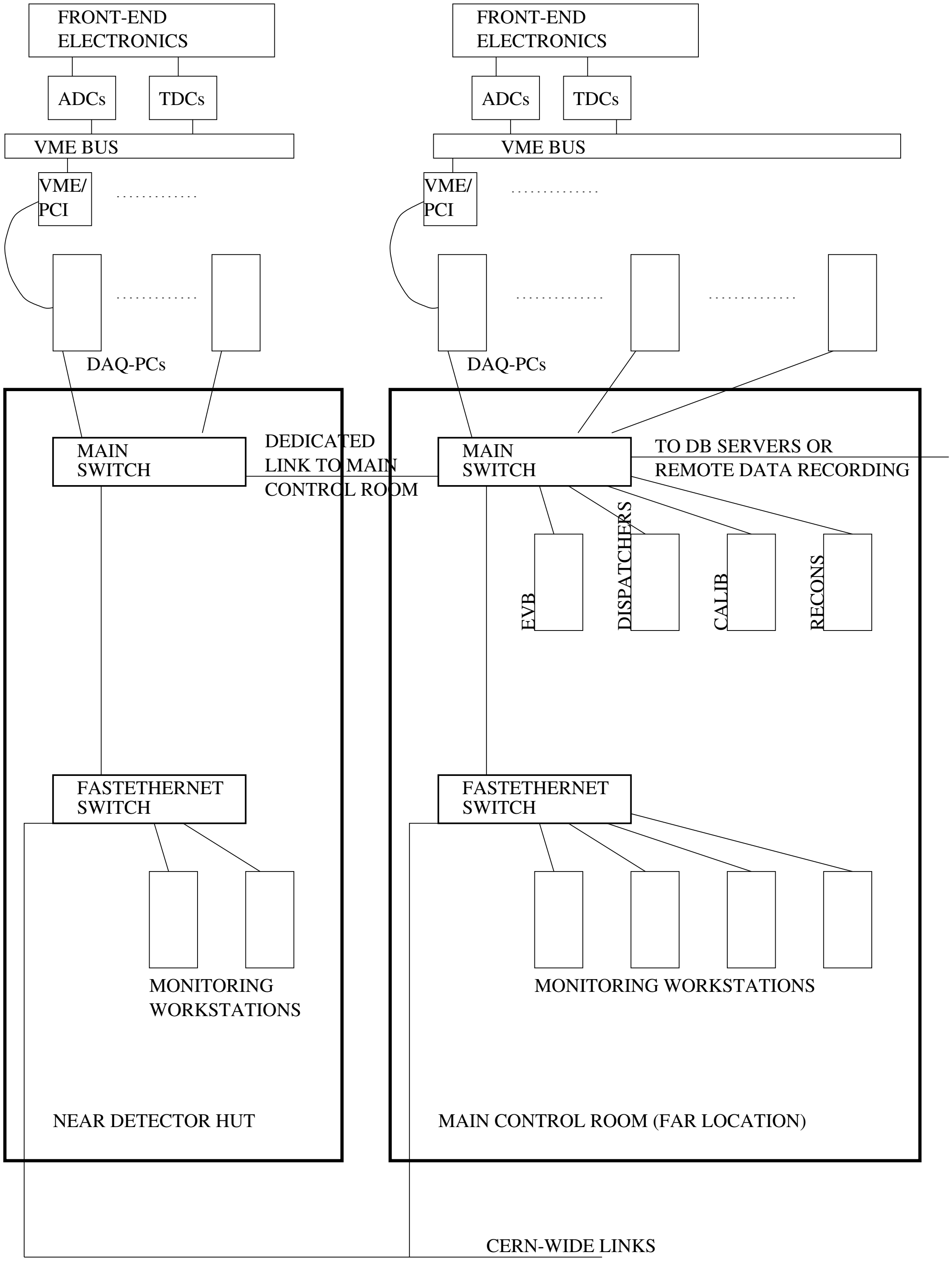

Figure 30: DAQ equipment and network topology

This mode of operation is useful to keep under control the preamplifier noise and the overall Common Mode Noise. A few events of this kind will be acquired during the time between bursts for periodic checks of pedestal and noise levels; these parameters are essential to define the discriminator threshold and to apply zero-suppression.

### 8.3.2 Absolute calibration

Absolute calibration with cosmic rays will take advantage of the presence of the TA chips. During the burst these chips provide time-stamping, while out-of-burst they are used for first level triggering.

The use of the TAs as trigger requires splitting of all the discriminator signals. On one side they will be sent to the TDCs; on the other side they will be fed to a summing logic, which will provide a global first-level trigger (T1) for a whole detector.

The arrival of a T1 signal will trigger the sequencer, which is able to perform independently the correct multiplexing sequence to the ADCs. At the same time, the discriminator pattern will be examined by a software T2 process to identify interesting patterns.

The T2 selection algorithm, based on a simple pattern recognition running on a single CPU, will be able to take a decision in a few tens of milliseconds. Hence, the total time needed after the arrival of a T1 trigger is of the order of 20 ms. This takes into account the multiplexing time (1 ms) and the estimated T2 decision time ($\approx$20 ms). A few more milliseconds must be added to transfer the data through ethernet when the decision is taken to read out the event. Based on these numbers we can rely on a T2 decision rate of approximately 50 Hz per CPU.

We estimate that the total rate of cosmic triggers in the detector will be approximately 10 kHz. Out of these we must select those cosmic muons oriented approximately as the detector axis. Accepting tracks in a cone opening by $\approx$ 30 degrees around the axis reduces the number of acceptable cosmic triggers to a few % of the total yield. We estimate the computing power in the readout PCs to be enough to get about 10 cosmic ray events with the desired characteristics per 1.2 s interburst.

All the calibration data will be processed by one or more dedicated PCs in the control room; calibration parameters will be constantly updated in the database.

## 8.4 Network Topology

The network will be organized around four ethernet switches as in figure 30. The driving idea is to have a switched fast-ethernet (100 Mbit/s) or gigabit ethernet backbone dedicated to the critical tasks, and to screen anything else behind fast-ethernet switches.

Gigabit ethernet is becoming commercially available. Its cost/performance ratio is still high compared to the relatively cheap fast-ethernet hardware. Should gigabit ethernet cost/performance improve before placing orders, we will evaluate its potential benefits in terms of speed and latency.

The readout PCs will be connected to the main switches to take advantage of the fastest possible network speed. One of these switches will be installed in each detector location. A dedicated connection will link the two switches to form the main backbone of the experiment.

Direct connection on the main backbone is foreseen for all the PCs that require the highest possible throughput and the minimum possible latency. These machines will most likely be the readout processors, the dispatcher, the event builder (EVB), the calibration processors, the run controller and the database server.

To isolate the DAQ traffic, which has highest priority, the monitoring tasks will be run on workstations connected to the backbone via a fast-ethernet switch. The link to the CERN-wide network will also be connected to the fast-ethernet switches. Firewalls will be needed to screen the backbone from unnecessary traffic from the outside.

## 8.5 Main DAQ process

The DAQ system will be logically organized around two dispatcher processes (see figure 31). A data dispatcher will be dedicated to the distribution of raw data to the EVB and to the calibration process. The other dispatcher will handle messages used by the run controller process to survey the operation of the whole system. The overall flow will drive all the data, including calibration parameters, from the readout processes to a database (DB).

The dispatcher concept has already been successfully used by the CHORUS collaboration for DAQ environments, both inside and outside CERN [45].

The only input to the data dispatcher will come from the readout processes on the DAQ PCs, which will send event blocks to the many processes waiting for raw data.

Three kind of processes will subscribe in read-only mode to the data dispatcher: the EVB, the calibration process and the monitoring tasks.

The EVB can be logically split into different processes. An event supervisor process can take care of the data integrity, checking the data stamping and allocating the necessary resources on the DB. A database writer process, controlled by the event supervisor, will push the raw data to the DB server, after having optionally performed a zero-suppression based on the actual calibration set. The latter will be fetched from the DB.

A calibration process will receive out-of-burst data and make all the necessary computations to keep an up-to-date calibration set in the DB. Since this operation will be performed periodically, the DB will contain, together with the raw data, the whole history of the calibration.

The monitoring tasks will be able to fetch data both from the dispatcher and from the DB, depending on the kind of checks they are performing.

One can foresee that reconstruction, event checking and event display processes will be running during data taking. These processes will be allowed to access data only from the DB.

The control dispatcher will provide bidirectional connection between all the processes taking part in the main data flow. It will be kept separate from the data dispatcher to increase the system stability. The run will be controlled by a DAQ supervisor and a run control. The impact of possible crashes in these critical tasks will be minimized by implementing these functionalities in distinct processes.

## 8.6 Database

A suitable choice for the database is Objectivity, which is currently studied for LHC data storage by the RD45 collaboration [46] .

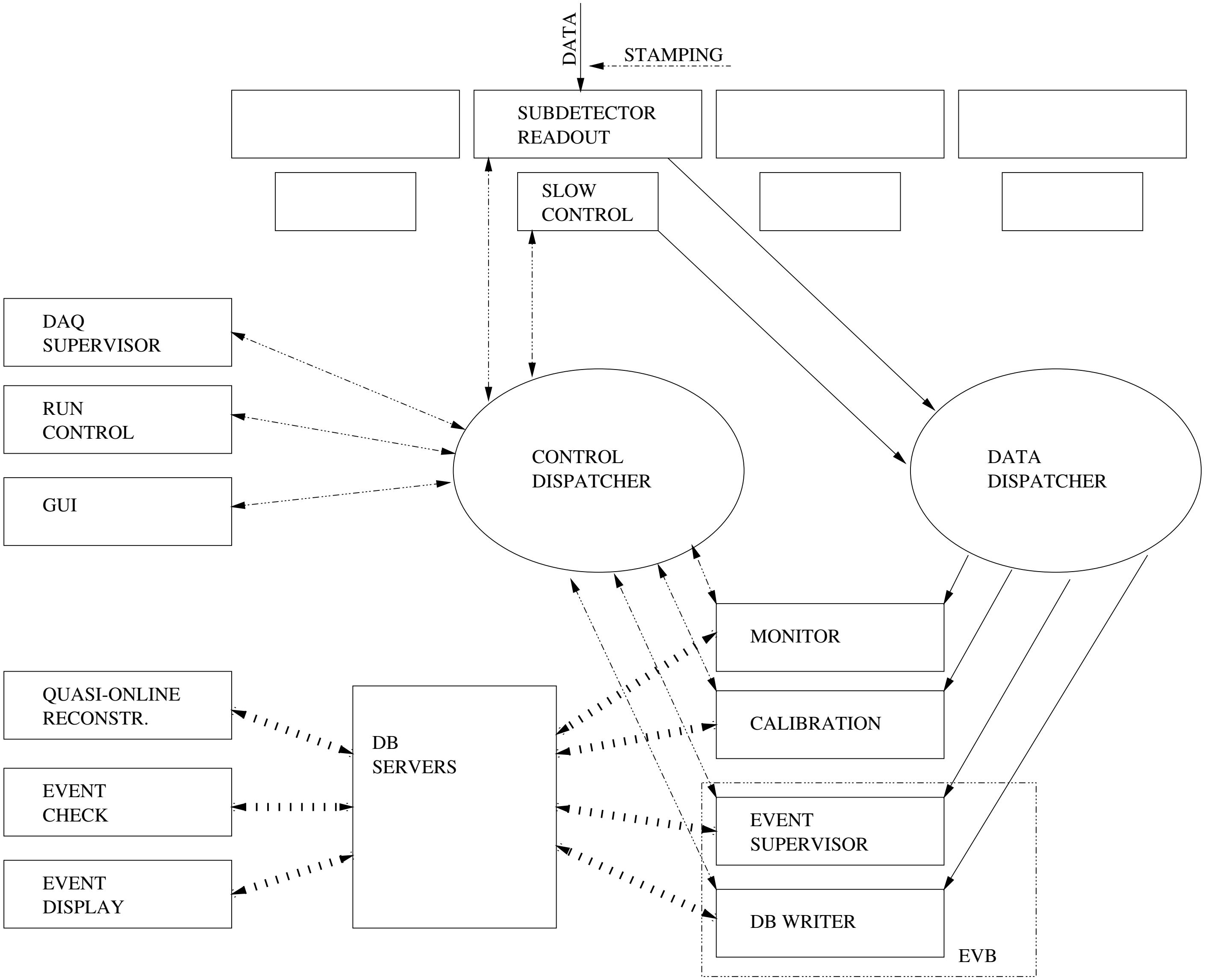

Figure 31: Main DAQ processes

Objectivity is already being used by the CHORUS collaboration for DAQ, storage and analysis of microscope data [47] .

## 8.7 Total Data Volume

Assuming 100% efficiency and 180 days running, the total yearly data volume would be approximately 4.5 TB before zero-suppression. The latter will squeeze the volume by at least a factor 10. When no zero-suppression is performed, a periodic download of database files to a remote data recording system must be foreseen; the rate will be about 1 GB/hour. When on-line zero-suppression is enabled, it may be even possible to keep all the data on local RAID disk arrays.

# 9 Signal and background

## 9.1 Low energy neutrino interactions

To evaluate the sensitivity of the experiment and the background contributions from different sources, events were generated using a simulation program that takes into account, in a phenomenological manner, experimental results available in the literature on neutrino interactions in the energy range of interest. The results of this simulation were compared with those obtained using other generators ([48] [49] [50] [51]) and excellent agreement was found among them.

The simulation includes specifically the quasi-elastic reaction $\nu_\mu \mathrm{n} \rightarrow \mu^- \mathrm{p}$ and, for both NC and CC reactions, the production of resonances and the onset of deep inelastic processes, with the proper energy dependence.

The energy distribution of neutrinos from the PS beam described in section 3 was used to generate the interactions. The absolute fluxes shown in fig. 5 and a cross section of $\sigma = 0.85 \times 10^{-38}\,\mathrm{cm}^2$ for the neutrino quasi-elastic scattering, measured in a comparable energy range [12], are the basis for the evaluation of the absolute normalisation and event rates computed in the following.

As already mentioned, the results of the simulation have been compared with experimental data. As an illustration, table 5 shows the abundance - relative to quasi elastic interactions - of various charged current topologies predicted by this simulation together with the values measured by a BEBC experiment [15, 52] in the same beam.

Table 5: Relative rates of charged current events: comparison with BEBC data [15].

| Interaction | BEBC(%) | Simulation(%) |
|---|---|---|
| $\nu\, n \rightarrow \mu^- p$ | 100 | 100 |
| $\nu\, p \rightarrow \mu^- p \pi^+$ | $40 \pm 4$ | 39.2 |
| $\nu\, n \rightarrow \mu^- p \pi^\circ$ | $23 \pm 3$ | 19.3 |
| $\nu\, n \rightarrow \mu^- n \pi^+$ | $15 \pm 3$ | 17.4 |
| $\nu\, n \rightarrow \mu^- p \pi^+ \pi^-$ | $10 \pm 2$ | 6.8 |
| $\nu\, p \rightarrow \mu^- p \pi^+ \pi^\circ$ | $8.5 \pm 2$ | 6.6 |
| $\nu\, n \rightarrow \mu^- n \pi^+ \pi^\circ$ | $5.0 \pm 1.6$ | 6.9 |

The fractions of charged and neutral current interactions in different final states containing at most two pions are shown in tables 6 and 7. The generator assumes an isoscalar target; it should be observed however that the iron and scintillator combination in the detector is such that $p/n = 1.055$ on average.

Since $\pi^\circ$ production in neutral current events is an unavoidable source of background to $\nu_\mathrm{e}$ quasi-elastic interactions, it is important that the ratio of neutral to charged current production of single $\pi^\circ$ events be reproduced correctly by the simulation. The Aachen-Padova collaboration [53] quotes for the cross section ratio

$$R_\circ = \frac{\sigma(\nu_\mu + N \rightarrow \nu_\mu + \pi^\circ + N')}{\sigma(\nu_\mu + N \rightarrow \mu^- + \pi^\circ + N')}$$

a value of $0.94 \pm 0.12$ which is in agreement with the result of $R_\circ = 1.06 \pm 0.10$ obtained in the simulation. The error on this latter number has been estimated from a comparison between the various generators mentioned above.

In conclusion we are confident that our generator gives a reasonable description of low energy neutrino interactions. We stress however that in the experiment the background subtraction will be based on measurements at the close detector and therefore will not rely on Monte Carlo descriptions of quantities such as $R_\circ$.

Table 6: Relative rates of different charged current interactions.

| final state | rate(%) |
|---|---|
| $\mu\,\mathrm{p}$ | 40.5 |
| $\mu\,\pi^+\,\mathrm{p}$ | 15.5 |
| $\mu\,\pi^\circ\,\mathrm{p}$ | 7.8 |
| $\mu\,\pi^+\,\mathrm{n}$ | 7.1 |
| $\mu\,\pi^+\,\pi^-\,\mathrm{p}$ | 2.8 |
| $\mu\,\pi^\pm\,\pi^\circ\,N$ | 5.3 |
| $\mu\,3\pi\,N$ | - |
| total CC | 79. |

Table 7: Relative rates of different neutral current interactions.

| final state | rate(%) |
|---|---|
| $\nu\,\pi^+\,\mathrm{n}$ | 3.0 |
| $\nu\,\pi^\circ\,\mathrm{p}$ | 3.0 |
| $\nu\,\pi^\circ\,\mathrm{n}$ | 3.0 |
| $\nu\,\pi^-\,\mathrm{p}$ | 3.0 |
| $\nu\,\pi^+\,\pi^\circ\,\mathrm{n}$ | 2.2 |
| $\nu\,\pi^+\,\pi^-\,N$ | 1.1 |
| $\nu\,\pi^-\,\pi^\circ\,\mathrm{p}$ | 1.1 |
| $\nu\,\mathrm{p}$ | 4.4 |
| total NC | 21. |

With the detector described in section 5 and the absolute flux from the simulation of the neutrino beam, $2.5 \times 10^{20}$ PS protons on target would yield a total of $3.48 \cdot 10^5$ quasi elastic $\nu_\mu$ interactions at the far location. The number of neutrino and cosmic ray (within the neutrino spill) events, at the two sites, are shown in table 8, together with the average rate per burst. [1] It can be observed that in the far detector the event rate is of order of 0.1 per burst while in the close calorimeter about one event per burst is expected. Furthermore, in this case, there will be a contribution from crossing muons, generated by neutrino interactions in the shielding, that has been estimated to be of the same order as the neutrino interaction rate.

The energy distribution of quasi elastic events, over the whole energy interval, is shown in fig. 32 for $\nu_\mu$ and $\nu_e$. The lepton spectra are shown in fig. 33 together with the momentum of $\pi^\circ$ produced in neutral current interactions.

---

[1] $\bar{\nu}_\mu$interactions - not listed in the table - increase the numbers by about 4%. The contribution of $\bar{\nu}_\mathrm{e}$will be included in the evaluation of the background.

Table 8: Number of events

| | FAR | CLOSE |
|---|---|---|
| $\nu_\mu$ Interactions | $8.6 \cdot 10^5$ | $8.4 \cdot 10^6$ |
| QE $\nu_\mu$ interactions | $3.48 \cdot 10^5$ | $3.41 \cdot 10^6$ |
| Cosmic Rays | $1.3 \cdot 10^5$ | $2.8 \cdot 10^4$ |
| Events/burst | 0.12 | 1.2 |

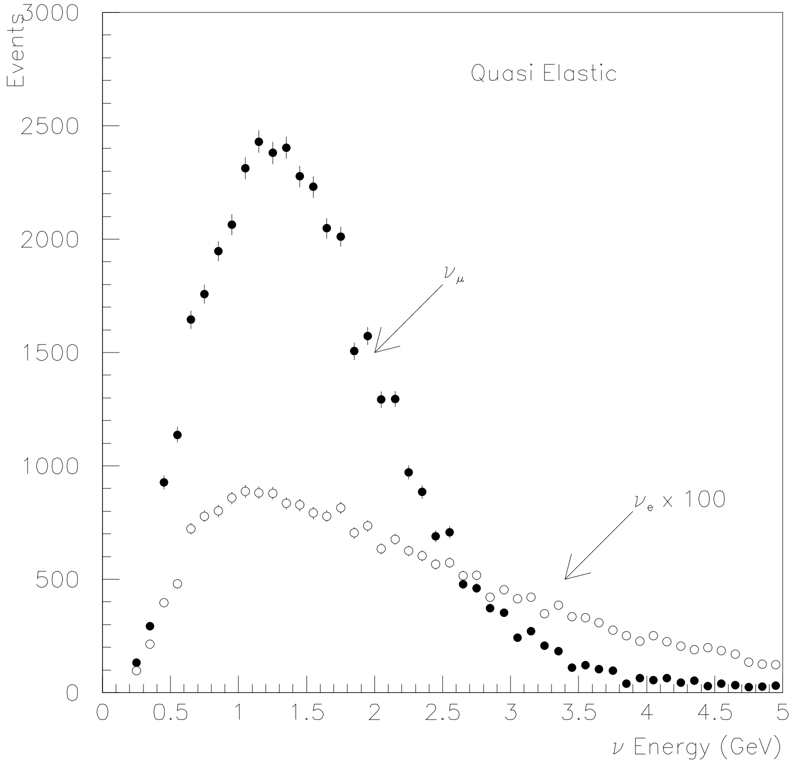

Figure 32: $\nu$ energy distribution for quasi elastic events.

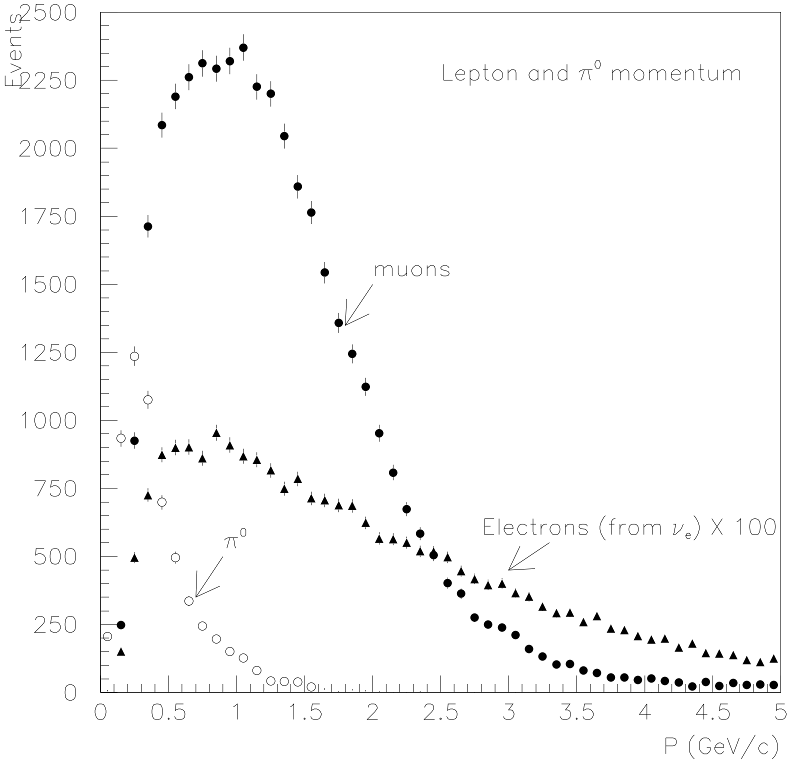

Figure 33: Lepton spectra in quasi elastic interactions compared with $\pi^\circ$ momentum in neutral current interactions. The spectra are normalised to the number of $\nu_\mu$ quasi elastic events.

# 10 Event simulation and selection

## 10.1 The detector simulation

We have performed a complete detector simulation, implemented within GEANT 3.21. The modular structure described in the section 5 was reproduced and scintillator bars of successive planes in the same projection were staggered by their half-width. The digitization of the detector signals was done by taking into account various effects: Birk's law for non linearity of the scintillator response, 3.5 m attenuation length of the WLS fibers, statistical fluctuations of the photoelectrons emitted from the photocathode. All these effects result in 10 photoelectrons being collected when a minimum ionizing particle crosses a bar parallel to the neutrino beam at the far end of the fiber, with no reflector. These data are compatible with the various laboratory tests performed. The simulation allowed to study the effect of reading the fibers from one side only with a reflector on the other end. Single side readout requires the capability to correct the signal of the strips for the attenuation length of the wavelength shifting fibers. This correction depends, in general, on the event topology and the distribution of hits in the detector. We checked, both on neutrino events and on single particles, that this correction can be applied efficiently by using the information recorded in the adjacent planes corresponding to the orthogonal projection.

Sets of data have been generated with and without an additional 2 mm thick layer of iron (0.11 $X_o$) following every scintillator plane. Most of the results presented in this section refer to the configuration with iron.

The simulation did not yet include the 0.5 mm thick aluminium foils used to pack the scintillator strips. However, this material corresponds to 0.01 $X_o$ per plane only. Moreover the insertion of thicker iron plates at the end of the calorimeter to absorb electromagnetic showers and muons was not considered in this simulation.

## 10.2 Event simulation and detector response

Different kinds of $\nu_e$ and $\nu_\mu$ interactions were generated according to the relative rates discussed in the previous section. We recall that the oscillation signal is represented by an excess of quasi-elastic $\nu_{\rm e}{\rm n} \to {\rm e}^-{\rm p}$ interactions with respect to the predicted rate measured in the near detector and normalized to $\nu_\mu$ quasi-elastic reactions. We show in figure 34 and 35 examples of these reactions as they appear in the detector. Figure 36 shows a generic neutral current interaction.

We have designed algorithms to determine the performance of the detector in measuring quantities related to the $\nu_{\rm e}$ quasi-elastic interactions. A good characterization of the electron shower is obtained by calculating plane by plane the centroid of the activity weighted with the pulse height of each bar. A linear fit through the centroids is then performed. Since in the case of $\nu_e$ interactions we expect most of the energy released around the fitted direction, we perform a second fit using only hits contained within a road of $\pm 15$ *cm* around the original fit. The result of the second iteration represents the measured direction of the electron. The vertex is then defined by the intercept of the shower axis with the first active plane of the event inside the road. The results of the application of the algorithm to $\nu_e$ quasi elastic event are shown in figure 37. The average resolution is 40 mrad for electrons of energies in the range 0.4 to 3.0 GeV. It is worth to mention that the performance of the algorithm is expected to improve once a specific treatment for the recoil proton is implemented.

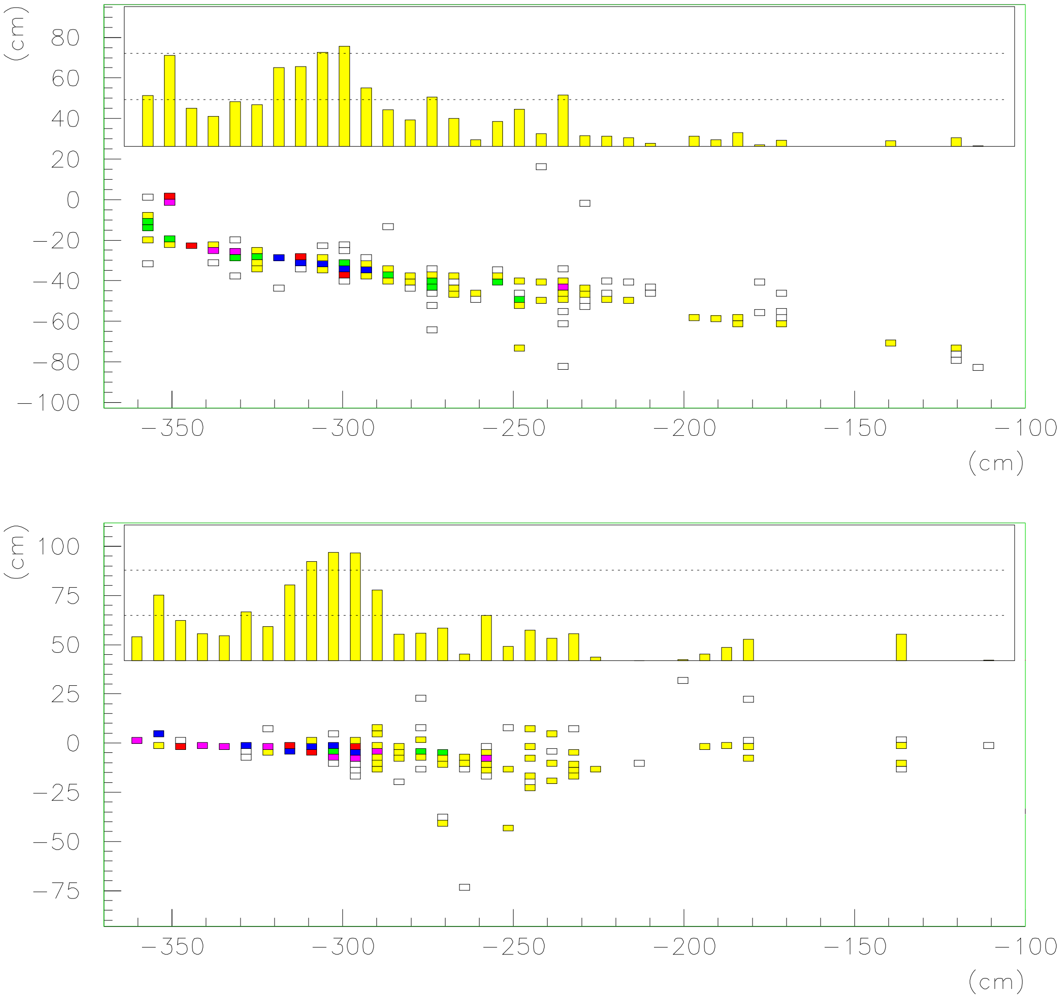

Figure 34: A $\nu_e$ quasi-elastic interaction ($E_\nu = 1.5$ GeV) shown in the two projections. The grey level in each square is proportional to the energy released in the corresponding scintillator bar. In the insets of the figures the sum of the pulse heights over the scintillator elements of each plane is displayed.

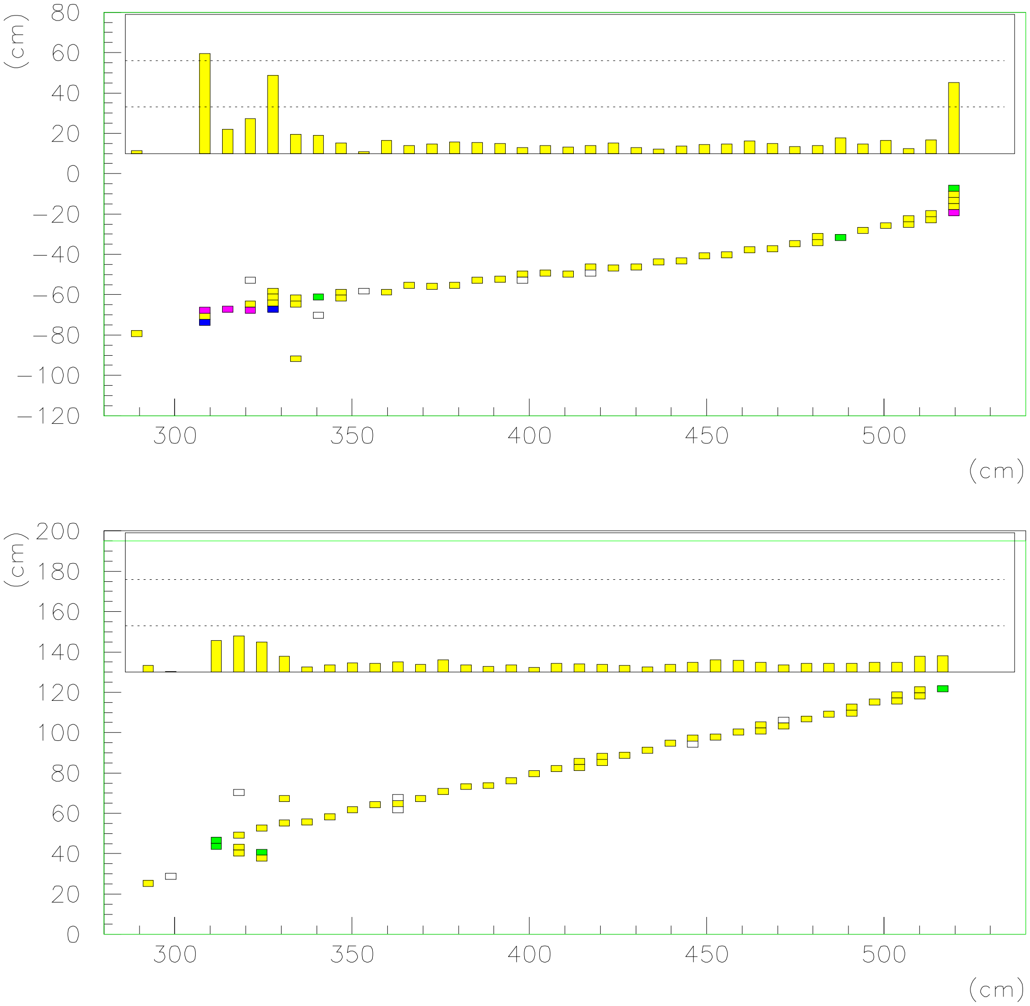

Figure 35: A $\nu_\mu$ quasi-elastic interaction .

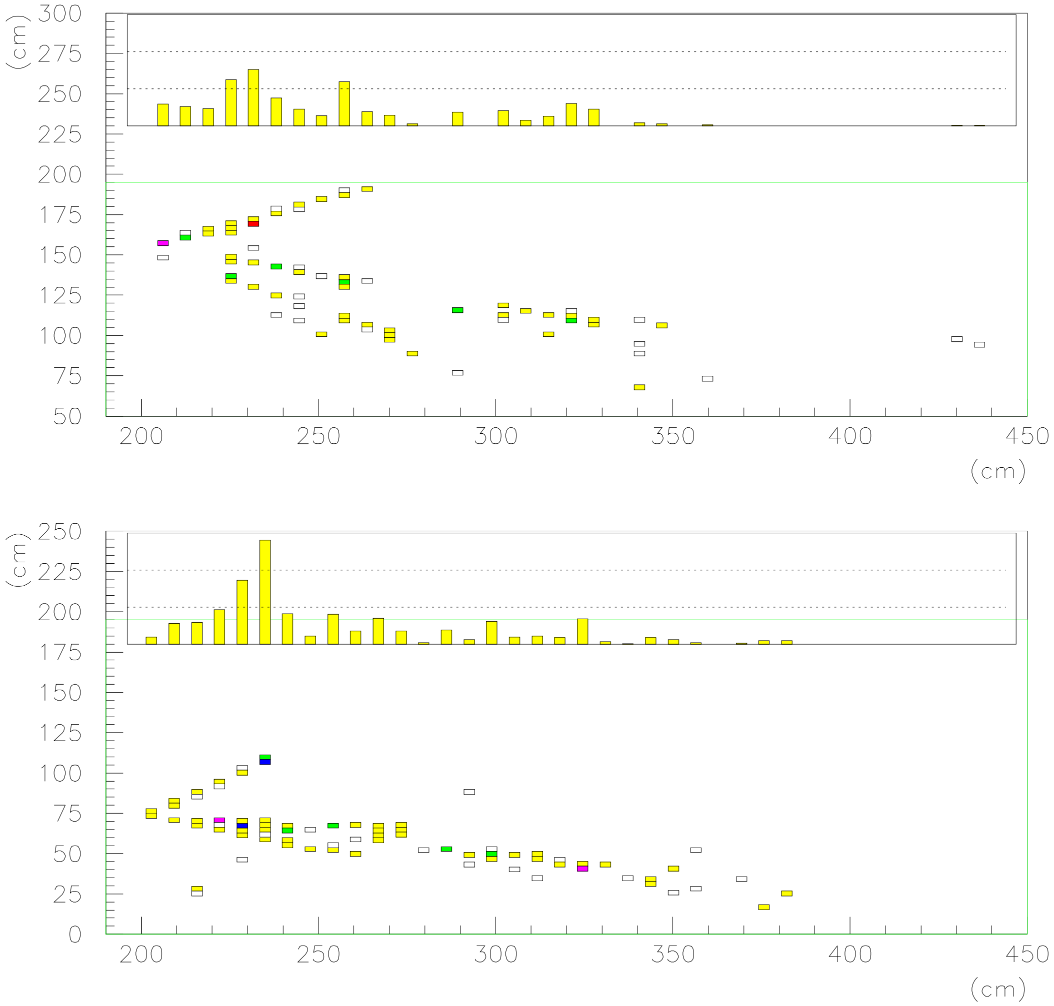

Figure 36: An example of a neutral current interaction.

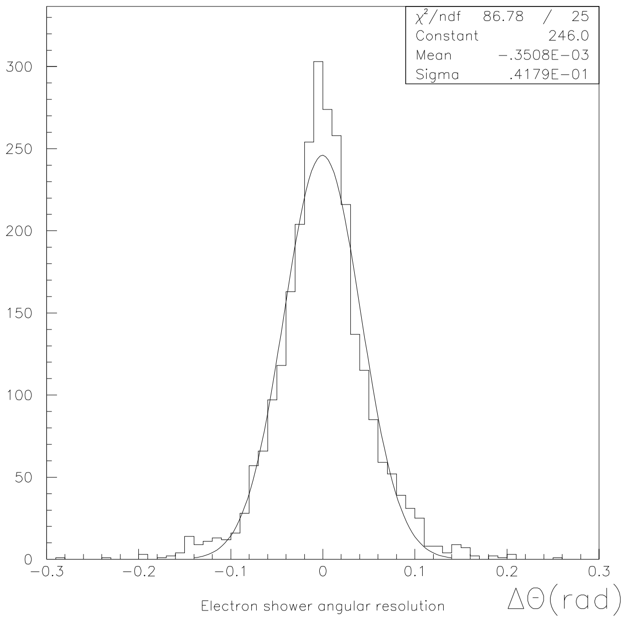

Figure 37: Angular resolution on electron direction in $\nu_\mathrm{e}$ quasi-elastic interactions

The reconstructed longitudinal position of the vertex is defined by the center of the first active plane. In more than 95% of the events the vertex is positioned in the right plane. The achieved resolution of the transverse vertex position is shown in figure 38.

The energy resolution on 1 GeV electrons is 7%. The electron energy from quasi-elastic interactions, combined with the direction measurement, can be used to reconstruct the incident neutrino energy with a relative resolution of better than 16% in the energy range considered.

## 10.3 Event selection

The number of events experimentally classified as $\nu_\mathrm{e}\mathrm{n} \rightarrow \mathrm{e}^-\mathrm{p}$ interactions (signal reaction) has contributions from the following sources:

- genuine $\nu_\mathrm{e}$ ( $\bar{\nu}_\mathrm{e}$ ) quasi elastic interactions, either from contamination in the beam or from $\nu_\mu \rightarrow \nu_\mathrm{e}$ ( $\bar{\nu}_\mu \rightarrow \bar{\nu}_\mathrm{e}$ ) oscillations;
- inelastic charged current interactions initiated by $\nu_\mathrm{e}$ in which some charged particles are not detected;
- $\nu_\mu \mathrm{e} \rightarrow \nu_\mu \mathrm{e}$ elastic scattering;
- neutral current interactions (initiated by $\nu_\mu$ or by $\nu_\mathrm{e}$) where electromagnetic activity (from $\pi^\circ$ decay) simulates the quasi elastic pattern;
- $\nu_\mu$ charged current interactions where the muon is not identified.

The main contribution to the background is expected to come from $\nu_\mu$ NC interactions with a $\pi^\circ$ in the final state. The number of events expected from elastic

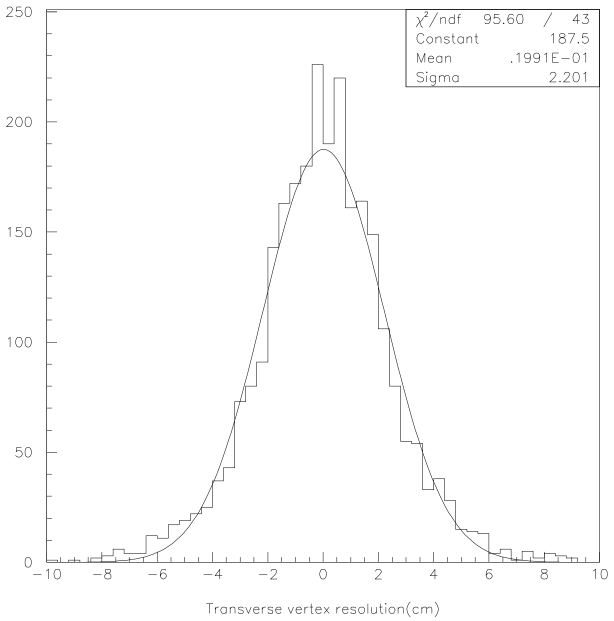

Figure 38: Precision on the determination of the transverse vertex position for $\nu_{\rm e}$ quasi-elastic interactions.

scattering of $\nu_\mu$ on electrons is one order of magnitude smaller than that due to the $\nu_{\rm e}$ and $\bar{\nu}_{\rm e}$ components of the beam and will therefore be neglected in the following.

As can be seen in figure 34, the electron from a quasi-elastic event shows the characteristic pattern of a narrow shower, with high energy deposition in the scintillator elements in the core of the shower. As a first step, $\nu_e$ candidates were preselected by a coarse filter program designed to remove events clearly incompatible with the presence of an electromagnetic shower. The algorithms were based on the global shape of an electromagnetic shower from a single isolated electron, as compared to the shower configuration typical of a neutral current event. Schematically the algorithms require:

- a minimum number of scintillator bars hit;
- a large ratio between the energy released inside and outside a $\pm\ 15cm$ radius cylinder along the shower direction determined as described earlier;
- a small transverse width with respect to. the electron direction

In addition we required the deposited energy per plane not to be consistent with a m.i.p. for an adequate number of planes in order to reject $\nu_\mu$ CC events.

As an example we show in figure 39 the radius of the cylinder around the electron direction containing 90% of the energy for $\nu_e$ quasi-elastics and for $\nu_\mu$ NC events. A cut at 50 $cm$ has an efficiency of 78% for electrons while rejecting 84% of NC interactions.

The resulting sample was scanned in order to evaluate the rejection power of more sophisticated pattern recognition algorithms. The dominant $\pi^\circ$ background is characterized by the fact that the electromagnetic activity is initiated by two photons with a significantly large opening angle. As a consequence, at the visual scan the $\pi^\circ$ events often appear as two distinct electromagnetic showers, or a single but “fat” electromagnetic shower, broader than that expected from a single electron.

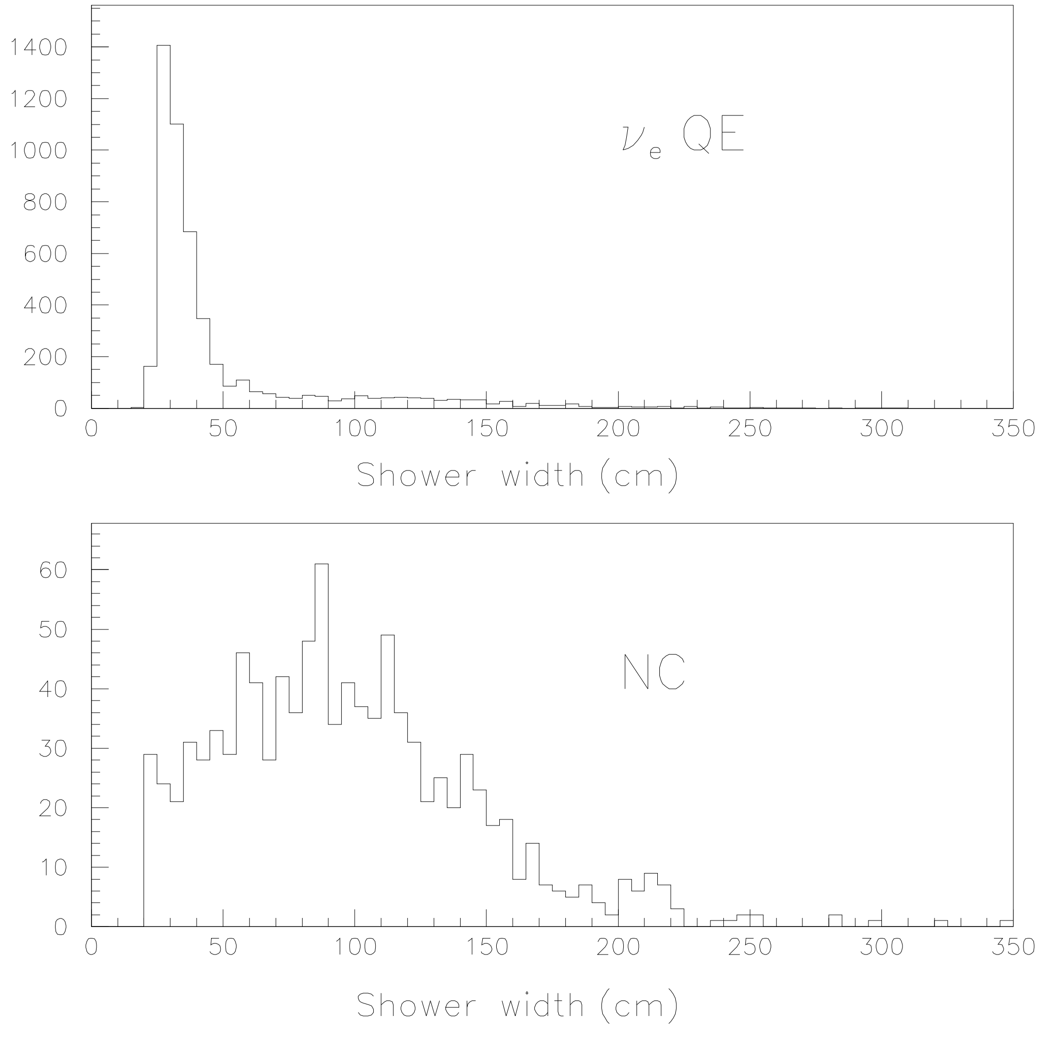

Figure 39: The 90% width around the electron candidate axis is shown for $\nu_e$ quasi-elastic events (top) and for $\nu_\mu$ NC events (bottom).

The analysis gave an overall efficiency of about 50% for signal events, with a signal to background ratio equal to 0.26 in the energy region 0.4 - 3.0 GeV. These values refer to an oscillation probability of 0.0031 and to large $\Delta m^2$ where the oscillated events have the same spectrum as the $\nu_\mu$ events. Background events are mainly produced by interactions of the $\nu_e$ component of the beam (47%), and by $\nu_\mu$ NC induced reactions (46%) while the contribution due to $\nu_\mu$ CC events turned out to be very small (7%). The quoted signal efficiency is computed by comparing the number of selected events with the total number of quasi-elastic interactions produced by oscillated neutrino in the detector at the far station. No extra factor for fiducial volume has therefore to be taken into account. We note that 30% of the selected events are due to deep-inelastic $\nu_e$ interactions. We also studied the energy dependence of the selection, which is used in the evaluation of the sensitivity to oscillation.

The analysis described above is referred to as "conservative detector performance" because no use was made of pulse height information in the early development of the shower. We are confident that such an analysis can reject the remaining $\pi^\circ$ background using the double m.i.p. signal from photon conversion versus the single m.i.p. of the electron track. Taking into account the very small thickness of the passive absorber ($0.11\ X_o$) of our calorimeter we expect to reduce the NC background by a factor of about 6. This makes this background component negligible compared to the irreducible background of the beam $\nu_e$ quasi-elastic interactions. The numbers quoted using this estimate are referred to as "expected detector performance". As will shown in section 11, however, the experiment sensitivity is moderately affected by this reduction factor.

In addition we note that another important handle not used in the present analysis is given by the possibility of exploiting kinematical constraints for the identification of quasi-elastic reactions.

In the near future, we plan to develop algorithms which include general pattern recognition and will replace the eye-scan by a full computerized procedure.

Finally, we note that the choice of iron as a passive material is motivated by its low cost. The optimization of the thickness and material of the absorber is also in progress.

# 11 Sensitivity to Oscillation

In this section we describe the sensitivity of the experiment to neutrino oscillations assuming the "expected detector performance" described in Section 10.

## 11.1 $\nu_\mu \rightarrow \nu_e$ oscillations in appearance mode

A comparison between the samples of charged-current $\nu_e$ events collected at the two detector locations will be made to search for neutrino oscillations. The charged-current interactions from $\nu_\mu$ neutrinos will be used as a normalization. The ratio of identified $\nu_e$ interactions and $\nu_\mu$ interactions will be measured at the close and the far locations. The difference between the ratios measured at the two locations provides a test of neutrino oscillations:

$$\Delta_e = \left(\frac{N_e}{N_\mu}\right)^{\text{far}} - C_e \left(\frac{N_e}{N_\mu}\right)^{\text{close}} \tag{6}$$

where $N_\mu$ is the number of events identified as $\nu_\mu$ interactions and $N_e$ is the number of events identified as $\nu_e$ interactions, including backgrounds. $C_e$ is a correction factor that takes into account the difference of the $N_e/N_\mu$ ratio at the two locations (see Section 3). Its value is close to unity with a systematic error of 3.5%. This will be the dominant systematic error on the measurement. The comparison of the two locations reduces the other systematic errors since the processes will be the same in the close and the far detectors.

In the absence of oscillations, the experiment would measure a value of $\Delta_e$ consistent with $\Delta_e = 0$. A measurement of a value of $\Delta_e$ significantly different from zero would be a sign for oscillations.

The $\nu_e$ candidates selected for the oscillation search have a measured neutrino energy between 0.4 GeV and 3.0 GeV. Figure 40 shows the expected distributions of the measured neutrino energy at the far location for $\Delta m^2 = 0.8$ eV$^2$ and $sin^2 2\theta = 0.007$. The distribution of the close detector, scaled by the ratio of muon events measured at the two locations ($N_\mu^{\text{far}}/N_\mu^{\text{close}}$), is also shown together with the distribution of oscillated $\nu_e$ events.

The $\nu_\mu$ candidates selected for the oscillation search have a measured neutrino energy between 0.6 GeV and 1.5 GeV. The selection efficiency of the $\nu_\mu$ charged-current events in this energy range is constant, which makes the normalization more robust.

Table 9 shows the expected number of events in the different samples for two years of data taking and two sets of oscillation parameters. In these two cases, that are representative of the region of parameter space favoured by LSND, the experiment would measure a value of $\Delta_e$ significantly different from zero. These two examples show that this result would be clearly inconsistent with the no-oscillation hypothesis at the level of 7.4 and 7.8 $\sigma$ respectively. When the energy distribution of the signal is used they are excluded by 10.7 and 11.3 $\sigma$ respectively.

Figure 41 shows the significance of $\Delta_e$ as a function of $\Delta m^2$ for $sin^2 2\theta = 0.007$. This measured quantity oscillates between positive and negative values depending on how many oscillated events there are at the two locations. It asymptotically goes to zero as the measured oscillation pattern in the 2 locations become equal. For this reason, the experiment is not sensitive to very large values of $\Delta m^2$. Figure 42 shows

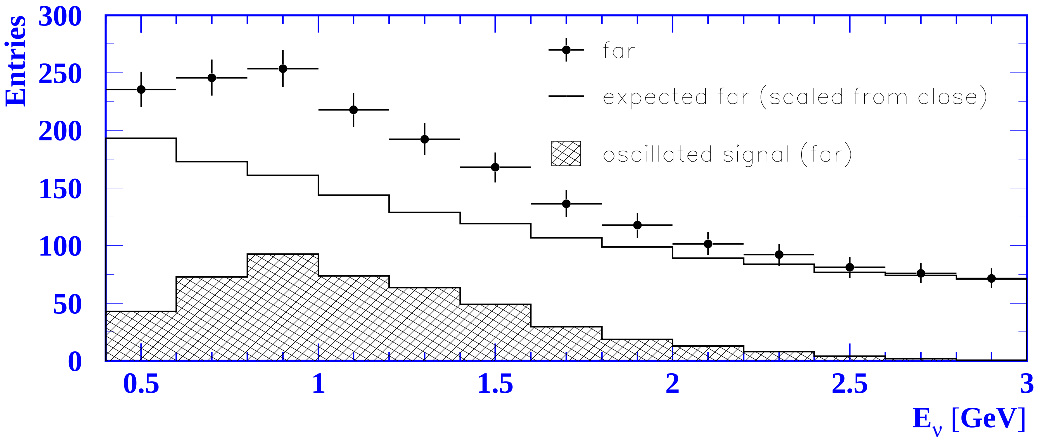

Figure 40: Distribution of neutrino energy of the signals in the close and the far detectors for $\Delta m^2 = 0.8$ eV$^2$ and $sin^2 2\theta = 0.007$. The errors shown are statistical. The data points represent the total signal at the far location. The curve represents the expected distribution at the far location, extrapolated from the close location. The histogram represents the oscillated $\nu_e$ signal.

Table 9: Expected events for two years of data taking. The errors on $\Delta_e$ are both statistical (first error) and systematic (second error).

| $\nu_e$ candidates | close | far |
|---|---|---|
| $\Delta m^2 = 0.8$ eV$^2$; $sin^2 2\theta = 0.007$ | 79 | 456 |
| $\Delta m^2 = 0.4$ eV$^2$; $sin^2 2\theta = 0.025$ | 71 | 487 |
| Total background | 12140 | 1200 |
| $\nu_\mu$ normalization | $8.8 \times 10^5$ | $8.7 \times 10^4$ |
| $\Delta_e$ ( $\Delta m^2 = 0.8$ eV$^2$; $sin^2 2\theta = 0.007$ ) | $(5.20 \pm 0.50 \pm 0.50) \times 10^{-3}$ | |
| $\Delta_e$ ( $\Delta m^2 = 0.4$ eV$^2$; $sin^2 2\theta = 0.025$ ) | $(5.50 \pm 0.50 \pm 0.50) \times 10^{-3}$ | |

the 90% confidence level exclusion plot expected if no signal and the expected background are observed. Two 90% CL exclusion contours are shown corresponding to the estimate of the $\pi^\circ$background both in the case of the “expected detector performance” and the “conservative detector performance”. The 90% and 99% exclusion plot computed for the “expected detector performance” are also shown in fig. 3. The energy spectrum information of the signal is taken into account in the calculation of the exclusion plot.

## 11.2 $\nu_\mu \rightarrow \nu_x$ oscillations in disappearance mode

The sample of contained muon events can also be used to study oscillations in disappearance mode, by comparing the samples of events with an identified muon at the close and the far locations. In the absence of oscillations, the number of events in the far detectors should be very close to the number of events in the close detector scaled

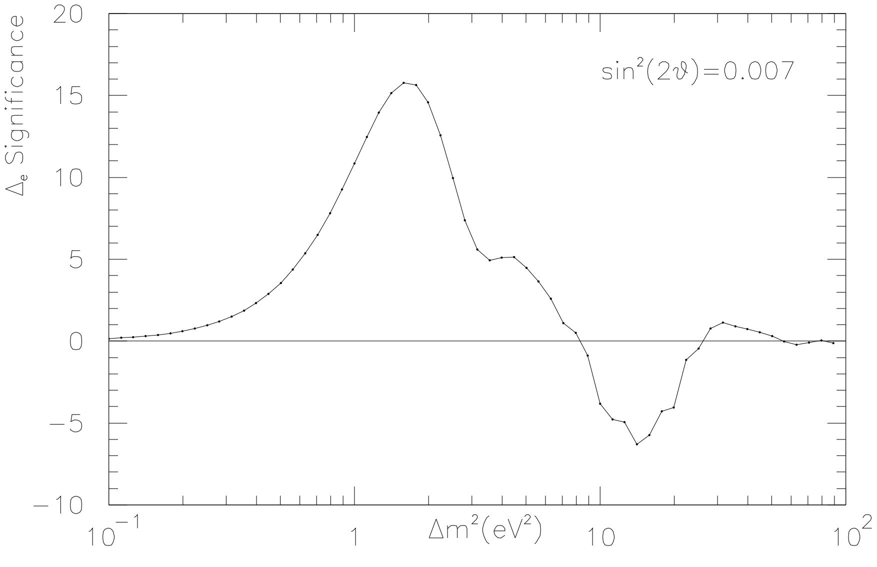

Figure 41: $\Delta_e$ significance, defined as the ratio between $\Delta_e$ and its error, as a function of $\Delta\mathrm{m}^2$ for $sin^2 2\theta = 0.007$, evaluated using the total number of the events in the experiment.

by the square of the ratio of the distances $(L_{\mathrm{close}}/L_{\mathrm{far}})^2$ and the ratio of the masses of the detector modules $M_{\mathrm{far}}/M_{\mathrm{close}}$. Measuring a value of

$$\Delta_\mu \quad = \quad N_\mu^{\mathrm{far}} - C_\mu N_\mu^{\mathrm{close}}, \tag{7}$$

significantly different from zero would be an indication for neutrino oscillations ($\nu_\mu \to \nu_{\mathrm{x}}$). The scaling factor $C_\mu$ takes into account the difference of the muon neutrino event rates at the close and the far locations; the value of $C_\mu$ can be determined with a relative precision of 3% as discussed in Section 3.

To be insensitive to the variations of the efficiency as a function of the muon energy, only muons having an energy above 0.6 GeV are considered. The efficiency of the selection of laterally contained quasi-elastic $\nu_\mu$ interactions is estimated to be $(39 \pm 1)\%$ and independent from the muon momentum. An upper cut on the muon energy at 1.5 GeV is also applied to ensure that all $\nu_\mu$ interactions within the fiducial volume have a longitudinally contained muon in the far detector. Although most of the selected events are $\nu_\mu$ quasi-elastic events, a contribution of the order of 20% of the sample will come from other charged-current $\nu_\mu$ interactions. As an example of signals, figure 43 shows the expected measured neutrino energy distributions for $\Delta\mathrm{m}^2 = 1.0$ eV$^2$ and $sin^2 2\theta = 0.1$.

Table 10 shows examples of measured number of events for given sets of oscillation parameters. The 90% confidence level exclusion plot is shown in figure 44. In disappearance mode, the experiment is limited by the systematic error on the difference of the beam spectra at the close and the far locations.

Our proposed experiment improves the sensitivity to $\nu_\mu$ disappearance by a factor $\sim 3$ with respect to CDHS [13] in the $\Delta\mathrm{m}^2$ region where LSND claims the $\nu_\mu \to \nu_e$ signal.

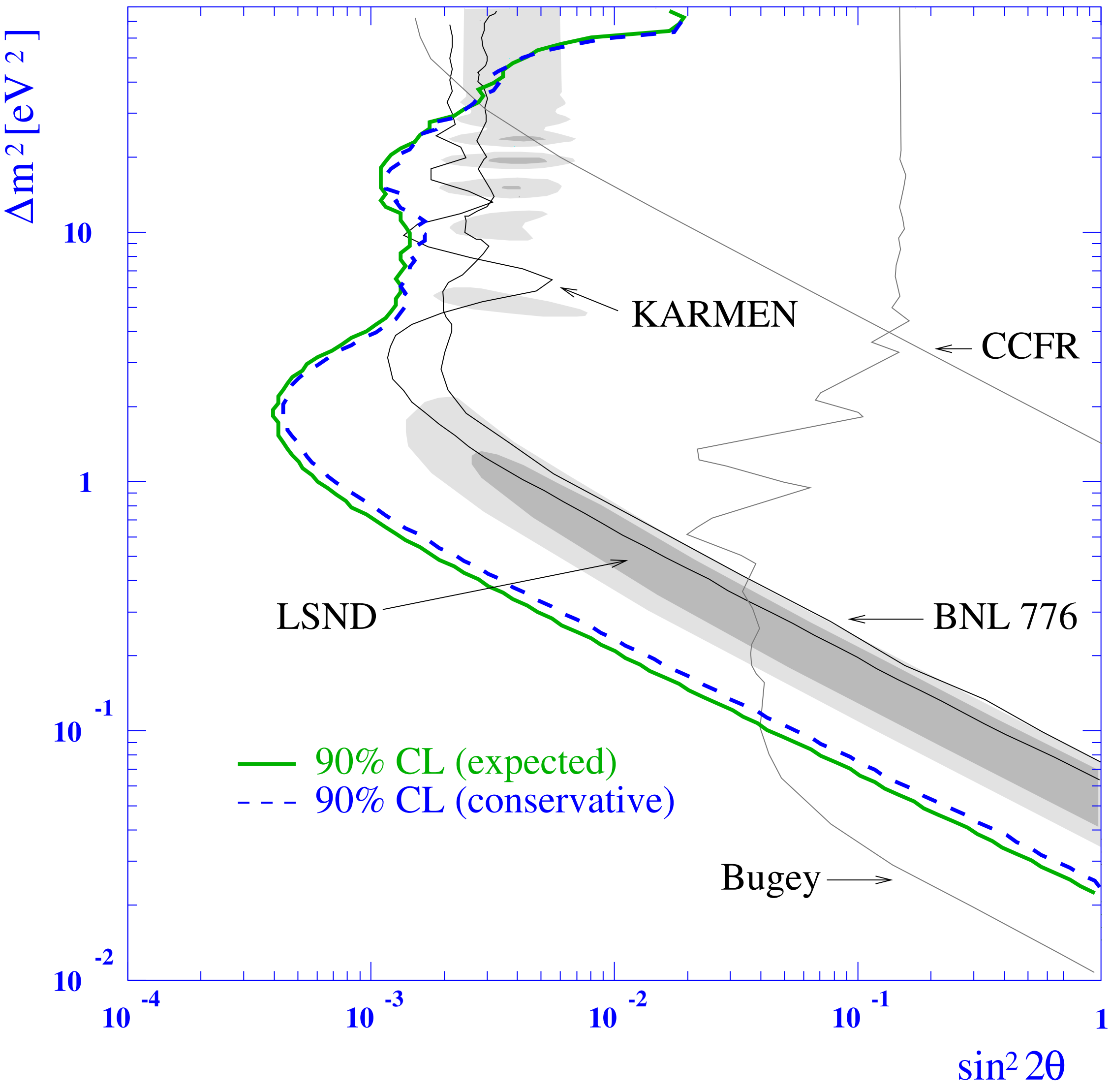

Figure 42: 90% exclusion plot for $\nu_\mu \rightarrow \nu_e$for the "expected detector performance" (solid line) and for the "conservative detector performance (dashed) evaluated using the energy spectrum of the events.

Table 10: Example of expected number of events identified as $\nu_\mu$ charged-current events in the close and the far detectors for two years of data taking. The errors on $\Delta_\mu$ are statistical (first error) and systematic (second error).

| parameters | $N_\mu^{\rm close}$ | $N_\mu^{\rm far}$ | $\Delta_\mu$ |
|---|---|---|---|
| $\Delta$m$^2$ = 1.0 eV$^2$; $sin^2 2\theta$ =0.1 | 880770 | 80910 | 6080 ± 300 ± 2600 |
| No oscillation | 882220 | 87130 | 0 ± 300 ± 2600 |

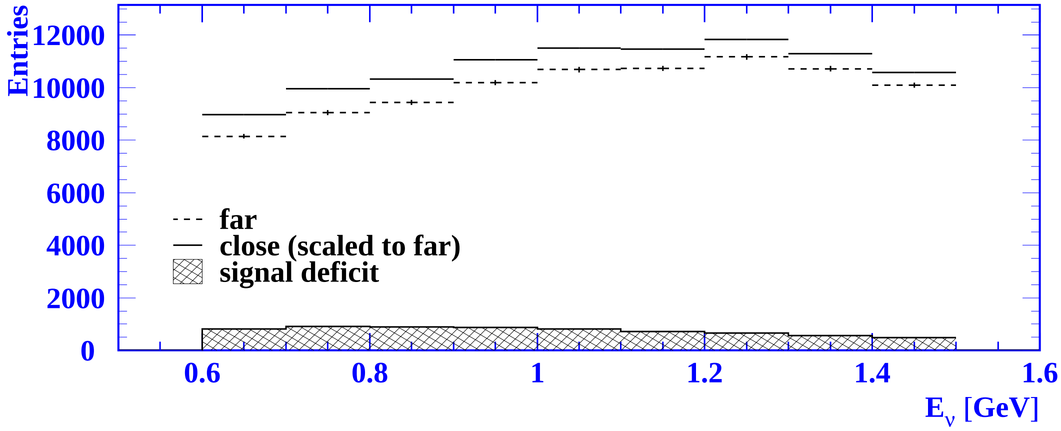

Figure 43: Shaded area: expected $\nu_\mu$ deficit for $\Delta\mathrm{m}^2 = 1.0$ eV$^2$ and $sin^2 2\theta = 0.1$. Full line: $\nu_\mu$ energy distribution at the far location as predicted by the near detector measurement in the absence of oscillation. Dashed line: $\nu_\mu$ energy distribution for $\Delta\mathrm{m}^2 = 1.0$ eV$^2$ and $sin^2 2\theta = 0.1$. The errors are statistical only.

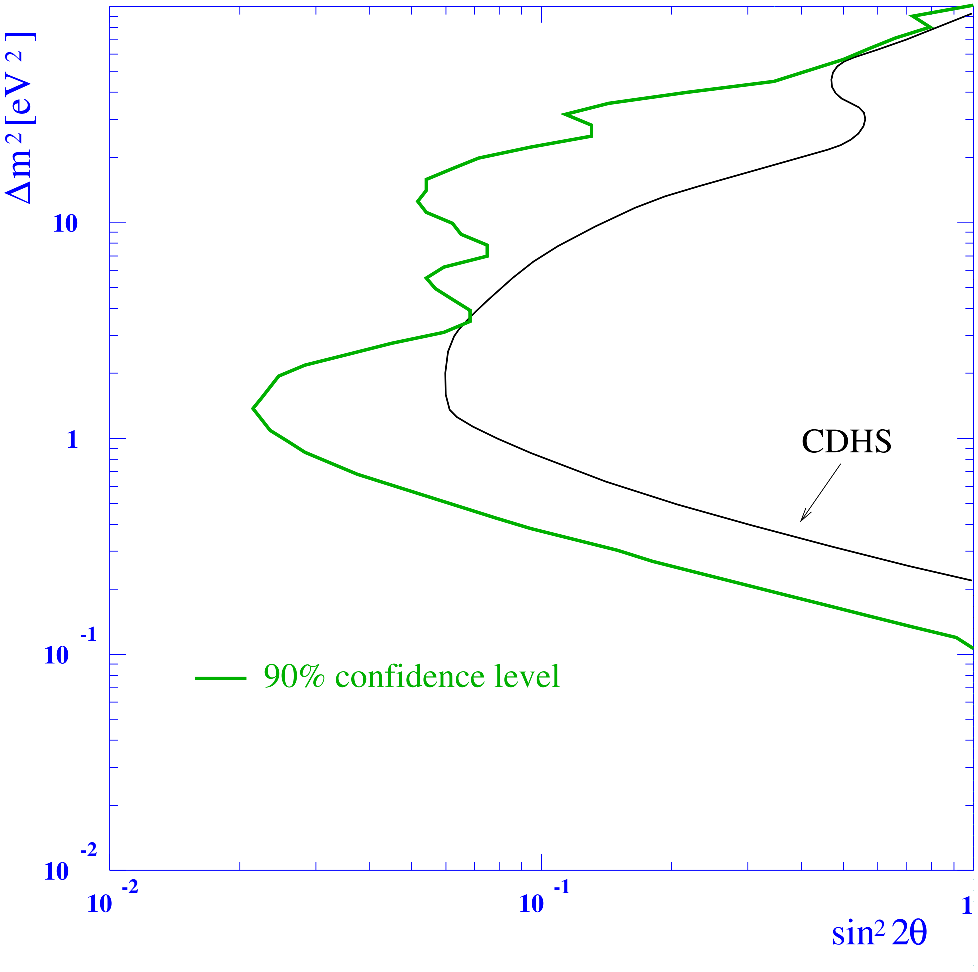

Figure 44: 90% exclusion plot for $\nu_\mu \to \nu_\mathrm{x}$.

## 11.3 The measurement of $\Delta$m$^2$ and $sin^2 2\theta$

In the event of a positive result in the LSND preferred region, the experimental issue becomes the determination of the oscillation parameters. For $\Delta$m$^2$ values above 1 $eV^2$, the excellent energy resolution of the detector allows the determination of the oscillation parameters with good precision. This is illustrated in figure 45a) where the 90% and $5\sigma$ contours are shown for the case $\Delta\mathrm{m}^2 = 2\ eV^2, sin^2 2\theta = 0.002$, still allowed by LSND.

Below $1\,eV^2$ the oscillation scales as $sin^2 2\theta \cdot \Delta m^4$. This implies that the individual oscillation parameters cannot be separated. Nevertheless, the significance of the positive result would be greater than $5\sigma$, as illustrated in figure 45b) for the $\Delta\mathrm{m}^2 = 0.8\ eV^2, sin^2 2\theta = 0.007$ solution.

For a positive result with an indication that $\Delta$m$^2$ is lower than 1 $eV^2$, the values of the parameters could be precisely measured with additional running time by lowering the momentum of the PS protons and by increasing the significance of the positive result through the suppression of the intrinsic beam $\nu_e$ contamination with the anti-tagging technique [55].

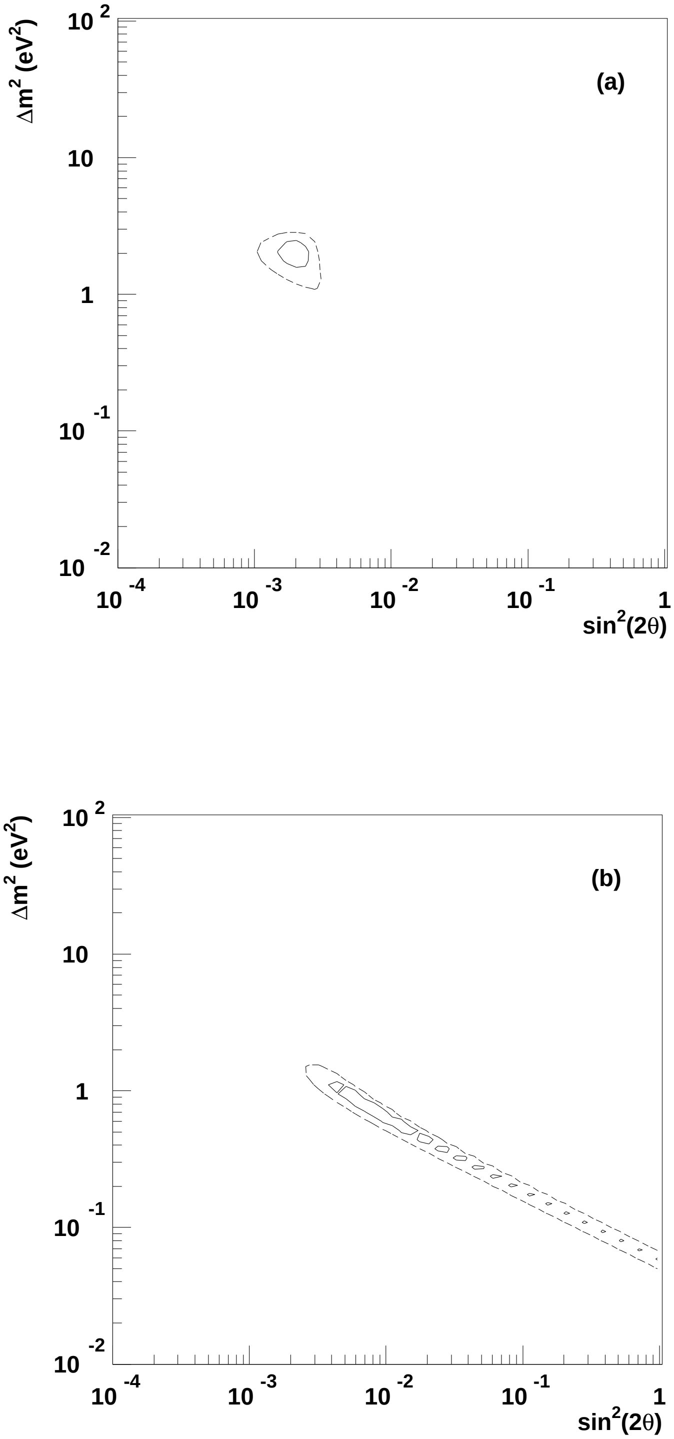

Figure 45: 90% (solid) and $5\sigma$ (dashed) CL signal plots for the $\Delta \mathrm{m}^2 = 2, sin^2 2\theta = 0.002$ solution, upper plot (a), and the $\Delta \mathrm{m}^2 = 0.8, sin^2 2\theta = 0.007$ solution (b).

# 12 Summary of cost

Table 11 displays a summary of costs, based on the detailed cost estimates given in the previous sub-sections. This table does not include the costs for the reactivation of the neutrino beam line presented in Section 3.5.

Table 11: Cost summary

| Item | Cost (MCHF) |
|---|---:|
| Detector basic units | 4.56 |
| 2mm Iron plates | 0.18 |
| End-System Iron plates | 0.40 |
| Multi-anode PMT's | 1.56 |
| High Voltage, Cables | 0.45 |
| Readout electronics | 0.93 |
| Data Acquisition | 0.30 |
| Exp. Hall Infrastructure | 0.16 |
| Contingency | 0.56 |
| Total cost | 9.10 |

We plan to ask the funding agencies of the collaborating Institutions to finance the construction in the ratio 30%,50%,20%, during the years 2000,2001,2002.

A possible scheme of the sharing of the requests between the different Institutions is contained in table 12. This scheme is preliminary because the required budget can still be slightly modified and because we expect to enlarge the collaboration in the near future.

Table 12: Requests for funding of detector construction

| | 2000 | 2001 | 2002 | total |
|---|---|---|---|---|
| BELGIUM | | | | |
| Brussels | 0.10 | 0.15 | 0.10 | 0.35 |
| Louvain | 0.10 | 0.15 | 0.10 | 0.35 |
| BULGARIA - Sofia | 0.03 | 0.03 | 0.03 | 0.10 |
| CERN | 0.40 | 0.80 | 0.30 | 1.50 |
| FRANCE - Paris | 0.10 | 0.20 | 0.10 | 0.40 |
| GERMANY - Berlin,Bonn | 0.10 | 0.20 | 0.10 | 0.40 |
| ITALY - Bari,Cagliari,Ferrara,Milano | | | | |
| Napoli,Padova,Roma1,Roma3,Urbino | 1.00 | 1.65 | 0.55 | 3.20 |
| JINR-Dubna | 0.07 | 0.07 | 0.07 | 0.20 |
| RUSSIA | | | | |
| Moscow | 0.07 | 0.07 | 0.07 | 0.20 |
| SPAIN - Valencia | 0.10 | 0.15 | 0.05 | 0.30 |
| TURKEY - Ankara | 0.07 | 0.08 | 0.05 | 0.20 |
| UNITED KINGDOM - Cambridge | 0.15 | 0.25 | 0.10 | 0.50 |
| USA | | | | |
| Michigan | 0.10 | 0.20 | 0.10 | 0.40 |
| South Carolina | 0.25 | 0.40 | 0.15 | 0.80 |
| Santa Barbara | 0.07 | 0.07 | 0.07 | 0.20 |
| Total | 2.70 | 4.47 | 1.93 | 9.10 |

# 13 Construction time scale

We estimate that six months of additional work are needed for further simulation studies and laboratory tests in order to finalize the detector design and place orders.

At the production rate of four basic units (one plane) per day at each of the four production sites, the total amount of time needed to build the three detector units is $\sim$ 200 working days. This is similar to the time estimated for building the readout electronics and for the procurement of the Multianode PMT's.

If the experiment is approved by the end of 1999, we are confident that useful data could be taken with part of the detectors as early as in the Fall 2001 and that the apparatus will be completed at the beginning of 2002, in time for the start of PS operation in March 2002 after the winter shut-down.

# Acknowledgments

We warmly thank R. Cappi, J.P. Riunaud, D. Simon and all the PS division staff for the work done investigating the possibility of restoring the PS neutrino beam line and providing to our experiment the required number of protons.

We acknowledge the important contributions from the technical staff of the various laboratories to the preparation of this proposal.

We would also like to acknowledge the help and support of N. Vassilopoulos in setting up the PS beam simulation program.

# References

[1] B. Cleveland et al., Astrophys. J. **496** (1998) 505;
V. Gavrin (SAGE Collaboration), Proc. XVIII Int. Conf. on Neutrino Physics and Astrophysics, Takayama (Japan, 1998), eds. Y. Suzuki and Y. Totsuka, to be publ. in Nucl. Phys. B.;
W. Hampel et al. (GALLEX Collaboration), Phys. Lett. **B447** (1999) 127;
M.R. Vagins (SuperKamiokande Collaboration), Proc. 29th Int. Conf. on High Energy Physics, Vancouver (Canada, 1998), eds. A. Astbury et al. (World Scientific, 1999), p. 596.

[2] M. Takita (SuperKamiokande Collaboration), Proc. 29th Int. Conf. on High Energy Physics, Vancouver (Canada, 1998), eds. A. Astbury et al. (World Scientific, 1999), p. 3.

[3] H. Gallagher (Soudan2 Collaboration), Proc. 29th Int. Conf. on High Energy Physics, Vancouver (Canada, 1998), eds. A. Astbury et al. (World Scientific, 1999), p. 579;
D.G. Michael (MACRO Collaboration), Proc. 29th Int. Conf. on High Energy Physics, Vancouver (Canada, 1998), eds. A. Astbury et al. (World Scientific, 1999), p. 584.

[4] C. Athanassopoulos et al. (LSND Collaboration), Phys. Rev. **C54** (1996) 2685; Phys. Rev. Lett. **77** (1996) 3082.

[5] C. Athanassopoulos et al. (LSND Collaboration), Phys. Rev. **C58** (1998) 2489; Phys. Rev. Lett. **81** (1998) 1774.

[6] G. Mills (LSND Collaboration), Results from LSND, presented at the XXXIV Rencontres de Moriond on Electroweak Interactions and Unified Theories, Les Arcs, France, 13-20 March 1999

[7] T. Jannakos (KARMEN2 Collaboration), Latest rResults from KARMEN-2, presented at the XXXIV Rencontres de Moriond on Electroweak Interactions and Unified Theories, Les Arcs, France, 13-20 March 1999

[8] L. Borodovsky et al., Phys. Rev. Lett. **68** (1992) 274.

[9] B. Achkar et al., Nucl. Phys. **B434** (1995) 503.

[10] E. Church et al., A proposal for an experiment to measure $\nu_\mu \to \nu_{\rm e}$ oscillations and $\nu_\mu$ disappearance at the Fermilab Booster: BooNE, proposal FERMILAB-P-0898 (1997).

[11] R.P. Thun and S. McKee, Phys. Lett. **B439** (1998) 123;
G. Barenboim and F. Scheck, Phys. Lett. **B440** (1998) 332;
G. Conforto, M. Barone and C. Grimani, Phys. Lett. **B447** (1999) 122.

[12] L. A. Ahrens et al., Phys. Rev. D31 (1985) 2732.

[13] F. Dydak et al., Phys. Lett. B134 (1984) 281.

[14] J. V. Allaby et al., Z. Phys. C40 (1988) 171

[15] C. Angelini et al., Phys.Lett. B179 (1986) 307.

[16] E. Church et al., LA-UR-97-2120, June 1997. “Neutrinos, Dark Matter and the Universe”, June 1996.

[17] Preliminary Feasibility Study and Cost Evaluation for an Experiment of Neutrino Oscillation at the CERN-PS, editor R. Cappi, PS/CA/Note 99-18 (tech.)

[18] G. Bernardi et al., Phys.Lett. B166 (1986) 47
P. Astier et al.,Nuclear Physics B335 (1990) 517-545

[19] D.Geigerat et al., Nucl.Instr. and Meth. A325 (1993) 92.

[20] The CNGS simulation program, NIM A 383 (1996) and CERN-SL/99-034, based on the experience of the West Area Neutrino Facility simulation programs.

[21] R.Cappi, J.P.Riunaud, D.Simon private communications and J.P.Riunaud, PS/CA/Note 99-19.

[22] I216 Letter of intent, CERN/SPSC/97-21, SPSC/I216, October 10, 1997

[23] CERN program library long writeup Q123, version 3.21, June 1993.

[24] J.V.Allaby et al., CERN/70-12 and reference therein.

[25] A. Ferrari and P. R. Sala, Proc. of the Workshop on Nuclear Reaction Data and Nuclear Reactor Physics, ICTP, Miramare-Triesten 1996, World Scientific p. 424, Vol I (1998)

[26] Work in progress with N. Vassilopoulos and A. Ball

[27] G. Bernardi et al., Phys. Lett. B166 (1986) 47

[28] P. Astier et al., Nucl. Phys. B335 (1990) 51

[29] J.V. Allaby et al., Z. Phys. C40 (1988) 17

[30] F. Dydak et al., Phys. Lett. B134 (1984) 28

[31] MINOS Collaboration, MINOS Technical Design Report, NuMi-L-337 TDR

[32] Pol.Hi.Tech s.r.l Strada Provinciale Turanense Km 44.400, Carsoli (AQ), Italy

[33] NuMi note L-250, NuMi note L-467

[34] Hamamatsu Photonics K.K.,325/6, Sunayama-CHO, Hamamatsu City, 430, Japan.

[35] Delft Electronic Products BV, P.O.Box 60 , NL 9300AB Roden, The Netherlands

[36] E. Ables et al., FERMILAB proposal P-875 (February 1995).

[37] G.Apollinari, P.de Barbaro and M.Mishina, “CDF End Plug Calorimeter Upgrade Project”, Fermilab-Conf-94/030-E, CDF note N2432. CDF Collaboration, “The CDF II Detector”, Technical Design Report. November 1996

[38] HERA-B Collaboration, Design Report, DESY-PRC 95/01, January 1995

[39] ATLAS collaboration, “Tile Calorimeter”, Technical Design Report, CERN/LHCC/96-42, ATLAS TDR 3.

[40] CMS collaboration, “Hadron Calorimeter Project”, Technical Design Report, CERN/LHCC/97-31, CMS TDR 2.

[41] CAEN SpA, Via Vetraia, 11 I-50049 Viareggio (Italy) info@caen.it, http://www.caen.it

[42] O.Toker et al. - VIKING, a CMOS low noise monolithic 128 channel frontend for Si-strip detector readout - NIM A 340 (1994) 572-579

[43] A.Duane et al. - Cherenkov rings detected with a multi-anode PMT - LHCB note 98/039

[44] *IDEas* - Frontend preamplifiers catalogue - http://www.ideas.no/VA_Manuals/VA_Table.htm

[45] R.Gurin, A.Maslennikov - CASPUR Consortium c/o Universita' la Sapienza, Rome, Italy.

[46] RD45 - A Persistent Object Manager for High Energy Physics - http://wwwinfo.cern.ch/asd/cernlib/rd45/index.html.

[47] O. Melzer - Data handling in the CHORUS emulsion experiment at CERN - Talk presented at HEP99, 15-21 July 1999.

[48] B. Blumenfeld, private communication.

[49] W.A. Lyle, Ph. D. Thesis, The Johns Hopkins University, 1989.

[50] S.Ricciardi, private communication.

[51] P. Lipari, M. Lusignoli, F. Sartogo, Phys. Rev. Lett. 74, 4384 (1995).

[52] R. C. Merenyi, Ph. D. Thesis, Tufts University, 1990.

[53] H. Faissner et al., Phys. Lett. B125 (1983) 230.

[54] F. Dydak *et al*, *Phys. Lett.* **134B**, 281-286 (1984).
F. Bergsma *et al*, *Zeit. f. Phys.* **C40**, 171-192 (1988).

[55] L. Ludovici, P. Zucchelli CERN-PPE/97-181, hep-ph/9701007, subm. to Nucl.Instr. and Meth.